

UNIVERSITY OF LEOBEN

**Sputtered TiN/Cu Multilayers and Nanocomposites:
Structure, Stresses and tribological Properties**

Diploma Thesis



by

ANNA M. HOFER


Leoben, June 2008

This thesis was supported by the Austrian NANO Initiative via a grant from the Austrian Science Fund FWF within the project "Stress Design" (N401-NAN).

Affidavit

I declare in lieu of oath, that I wrote this thesis and performed the associated research myself, using only literature cited in this volume.

Leoben, June 2008


Anna M. Hofer

Acknowledgements

I would like to thank o.Univ.-Prof. DI Dr. Helmut Clemens, head of the Department of Physical Metallurgy and Materials Testing, for giving me the opportunity to conduct this work at his institute.

My sincere gratitude is due to ao.Univ.-Prof. DI Dr. Christian Mitterer, head of the Thin Films Group at the Department of Physical Metallurgy and Materials Testing, for his supervision and for sharing his expertise with me, and to Priv. Doz. Dr. Jozef Keckes leader of the "Stress Design" Project.

I am much obliged to my supervisor and friend DI Dr. Harald Köstenbauer for his advice and for his patience while answering all my questions. Thanks for all the coffee breaks!

Sincere thanks to all members of the Thin Films Group and of the Department of Metallurgy and Materials Testing, who all supported my work. Special thanks go to DI Dr. Gerardo Fontalvo for his great support towards the end of the thesis and to DI Dr. Michael Panzenböck, who never lost his confidence in me and encouraged me to finish my studies.

Finally, I am very grateful to my family, my friend and colleagues. Without their help and support pursuing my studies would have been much more effort.

CONTENTS

| | | |
|----------|--------------------------------------------------------------|-----------|
| 1 | INTRODUCTION | 1 |
| 2 | DEPOSITION FUNDAMENTALS | 3 |
| 2.1 | GENERAL | 3 |
| 2.2 | PLASMA | 5 |
| 2.2.1 | Glow Discharge | 8 |
| 2.3 | SPUTTERING | 9 |
| 2.3.1 | DC - Sputtering | 9 |
| 2.3.2 | Magnetron Sputtering | 10 |
| 2.3.3 | Reactive Sputtering | 12 |
| 2.4 | THIN FILM GROWTH | 12 |
| 2.4.1 | Nucleation and Growth | 12 |
| 2.4.2 | Structure Zone Models | 14 |
| 3 | HARDENING MECHANISMS | 17 |
| 3.1 | STRENGTHENING BY GRAIN SIZE REDUCTION AND SIZE EFFECTS | 19 |
| 4 | THERMALLY ACTIVATED PROCESSES..... | 23 |
| 4.1 | DIFFUSION | 23 |
| 4.2 | RECOVERY AND RECRYSTALLISATION | 24 |
| 4.3 | THERMALLY ACTIVATED PROCESSES IN PVD COATINGS..... | 25 |
| 5 | RESIDUAL STRESSES..... | 26 |
| 5.1 | GROWTH STRESSES IN POLYCRYSTALLINE FILMS..... | 26 |
| 5.2 | SUBSTRATE CURVATURE | 27 |
| 6 | TRIBOLOGICAL PROPERTIES | 30 |
| 6.1 | FRICITION | 31 |
| 6.2 | WEAR | 32 |

| | | |
|----------|-----------------------------------------------------|-----------|
| 7 | EXPERIMENTAL | 34 |
| 7.1 | COATING DEPOSITION | 34 |
| 7.1.1 | Coating Facility | 34 |
| 7.1.2 | Deposition Procedure | 35 |
| 7.1.3 | Substrates and Targets..... | 36 |
| 7.1.4 | Coating Deposition Parameters | 36 |
| 7.2 | COATING CHARACTERISATION | 38 |
| 7.2.1 | Coating Adhesion | 38 |
| 7.2.2 | Coating Thickness | 39 |
| 7.2.3 | Scanning Electron Microscopy (SEM)..... | 40 |
| 7.2.4 | X – Ray Diffraction Analysis (XRD)..... | 40 |
| 7.2.5 | Transmission Electron Microscopy (TEM)..... | 41 |
| 7.2.6 | Evaluation of Micro Hardness..... | 42 |
| 7.2.7 | Biaxial Stress Temperature Measurement (BSTM) | 44 |
| 7.3 | TRIBOLOGICAL TESTING..... | 45 |
| 7.3.1 | Friction | 45 |
| 7.3.2 | Nanofocus Analysis..... | 46 |
| 8 | RESULTS AND DISCUSSION | 47 |
| 8.1 | BI-LAYER AND MULTILAYER | 47 |
| 8.1.1 | Structure | 47 |
| 8.1.2 | BSTM | 51 |
| 8.2 | NANOCOMPOSITE | 54 |
| 8.2.1 | Structure | 54 |
| 8.2.2 | BSTM | 59 |
| 8.2.3 | Tribological Behaviour..... | 60 |
| 8.2.3.1 | Room temperature | 61 |
| 8.2.3.2 | Tribological behavior at 300° C and 500° C | 65 |
| 9 | SUMMARY AND CONCLUSION | 69 |

1 Introduction

In the last decades there have been remarkable advances in coatings technology. Hard coatings are applied to extend lifetime of cutting tools and dies and in many applications to minimise wear. Thermal coatings are used in gas turbine engines to enhance the performance and to protect compressor and turbine components. Protective coatings, which "defend" the substrate material from gaseous and aqueous environments, are exerted in chemical industries, coal gasification plants and nuclear reactors. All these coatings have extremely high hardness, very high melting points and resistance to chemical attack in common [1].

The bond structure of a hard coating determines its properties. There are three types of hard coating material depending on the nature of the bonding. First there are *ionic* hard oxides (Al_2O_3 , ZrO_2 , TiO_2), second are *covalent* hard materials (diamond, B_4N , SiC , Si_3N_4) and finally are *metallic* hard compounds (TiN , TiC , WC)[2]. In particular transition metal nitrides (e.g. TiN) are known for their high hardness, excellent wear resistance, chemical inertness and good electrical conductivity. Therefore, they have been the most studied and investigated compounds ever since the beginning of the use of hard coatings [1, 3].

Mechanical industry, however, makes high demands on their tools which cannot be fulfilled immediately. To satisfy these permanent requests, new hard coatings have to be developed. The development of a very fine microstructure (so called nanostructured materials) is crucial to enhance coating properties. Mainly three factors influence the microstructure: deposition temperature, pressure and degree of ion bombardment. An increase of deposition temperature leads to a denser structure as shown by structure zone models. Alternatively, ion bombardment can be provided by the application of suitable bias to the substrate. The higher the bombardment rate is, the denser the structure of the growing film due to filling of voided boundaries. Furthermore, ion bombardment leads to considerable compressive stresses which results in improved hardness. Generally, compressive stresses are also desired as they can hinder crack formation or crack growth [4, 5].

Nowadays for development of advanced hard coatings it is of major importance how microstructural engineered and compositionally modulated films are influenced by thermal processes [6]. With the knowledge about structural behaviour of coatings, tailored properties for the fields of application are feasible.

Nanocomposite coatings consist of at least two different phases. A low fraction of a metal segregating at the grain boundaries of e.g. TiN can be used to realize hard and superhard coatings, as has been proposed by Vepřek and Reiprich [7, 8]. This behaviour has been shown e.g. for ZrN/Cu [9]. Information about stress relaxation at elevated temperatures in such a nanocomposite is still very limited. Investigations regarding this topic have been conducted by Köstenbauer et al. [10]. Furthermore, soft metal phases combined with a hard compound in

a nanocomposite structure show improved tribological properties. Influences of multilayer structures or superlattices (periodicity is in nanometer range) on stress formation is yet not fully understood [11]. There is a very limited number of publications available in literature on this topic. For example, stress/temperature behaviour of multilayered TiN/Ag coatings has been studied by Köstenbauer et al. [12].

This thesis presents multilayered and nanocomposite structures of TiN/Cu films deposited by sputtering. Structural investigations, stress relaxation due to thermal cycling and tribological behaviour have been investigated. For tailored coatings, the correlation between film structure and resulting stresses in the as-deposited as well as in the annealed state is of major importance. Furthermore, the understanding of stress relaxation behaviour during thermal cycling leads to increased lifetime of thermally loaded tools. Finally, tribological investigations have been conducted for nanocomposite coatings.

2 Deposition Fundamentals

2.1 General

The surface has great impact on the behaviour of a solid. Since many decades, people have been trying to modify the surface of bulk materials in order that it can resist environmental influences. These influences can be corrosion, chemical exposures and mechanical, thermal, and electrical loads. Even very thin layers are able to enhance the lifetime of a tool enormously. In practise, such layers are often used to minimise friction and wear of cutting tools.

There are different ways to apply protective coatings. Some of them have been used for over hundreds of years like enamelling, case hardening or galvanising. Others have been developed in the last century such as surface welding or thin film application. This diploma thesis is about the behaviour of thin TiN/Cu films. Therefore, the theoretical part is restricted to the deposition methods of thin films. There are several fabrication methods of thin coatings which can be classified in different ways. One possibility is given here [13]:

- *Wet Processes*: the deposition material is transported in liquid state
 - Electroplating Deposition
 - Electroless Plating Deposition
 - Anodic Oxidation Deposition
 - Sol Gel Deposition

- *Dry Processes*: the deposition material is transported in vapour phase
 - Chemical Vapour Deposition (CVD)
 - Physical Vapour Deposition (PVD)
 - Oxidation Deposition

Each of these methods has its characteristic field of application which is expanded by continuous research. The methods most commonly used for thin film application are PVD and CVD. The advantages of the PVD process are higher deposition rates at lower deposition temperatures, whereas the throwing power is better in the CVD process [14]. Thin films produced by PVD processes are used for optical, opto-electronic and magnetic applications as well as protection against wear and corrosion. The coatings deposited within this work were done by PVD. Therefore, only this method will be described more precisely.

There are four main PVD methods of industrial relevance:

- Evaporation
- Ion Plating
- Sputtering
- Cathodic Arc Evaporation

Evaporation

The basics of the evaporation process consists in heating up the coating material (target) in vacuum ($10^{-3} - 10^{-6}$ Pa) until the atoms on the surface are vaporised (see Figure 2.1). These atoms condense then on the cooler substrate surface and form the coating.

Sputtering

A plasma is ignited between the cathodic target and the anodic substrate. The ions of the plasma accelerate towards the target (coating material) and strike its surface as depicted in Figure 2.1. In this way, atoms, ions and clusters are dislodged and deposited on the substrate, to which a more positive potential compared to the target is applied [15].

Ion Plating

The coating material is vaporised in vacuum similar to the evaporation process. In addition, a positive potential is applied to the vaporisation source. The vaporised material passes through the plasma, which is ignited between the vacuum chamber and the substrate, and is thereby ionised (see Figure 2.1). Due to the negative potential applied to the substrate, the ions accelerate and discharge by hitting the substrate. The coating is bound very strongly to the substrate by using this technique [16].

Cathodic Arc Evaporation

Basically, a high-current low-voltage arc is ignited which melts and evaporates the cathode material (target) [17]. This highly ionised material flow moves towards the substrate and condenses at the surface. The advantage of this method is a dense film which is strongly bonded to the substrate due to the high energies of the vapour [18].

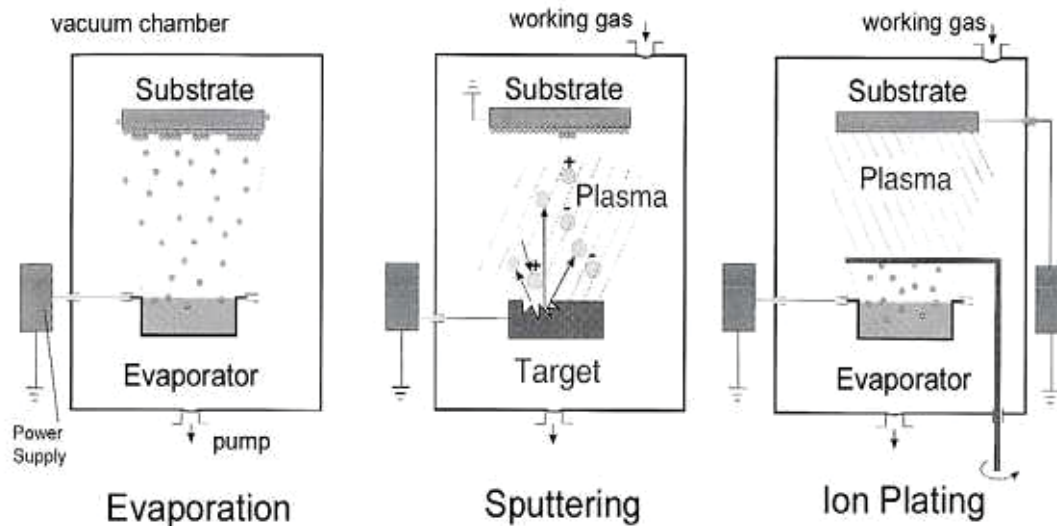


Figure 2.1: Delineation of the three basic PVD processes [modified after 15]

Additionally, in all processes described above, a reactive gas (e.g. N_2 , O_2) can be introduced to the chamber in order that a reaction between the gas and the vaporised material can take place. In this way, a compound different from the target material can be deposited. For these methods, the ratio of the partial vapour pressure and the reactive gas partial pressure can only be determined in experimental ways and is very important for all properties of the coating [19].

2.2 Plasma

Besides solid, liquid and gas, plasma is energetically the fourth state of matter. It exists in natural form in the cosmos or is generated under unique conditions for specific purposes (see Figure 2.2). Nowadays, plasma is indispensable for surface engineering, and film properties can be enhanced by changing the plasma characteristics [20].

In general, plasma can be seen as an ionised gas. In a more decisive way it can be defined as a *quasi neutral gas* of charged and neutral particles characterised by a *collective behaviour*. Quasi neutral means that there are approximately as much negative as positive charge carriers in a sufficient expanded area. In plasma, the motion of these particles can cause local concentrations of positive and negative electrical charges. Thus, long-ranged Coulomb fields are caused which influence the motion of other charged particles far away, which is the denotation of collective behaviour [21, 22].

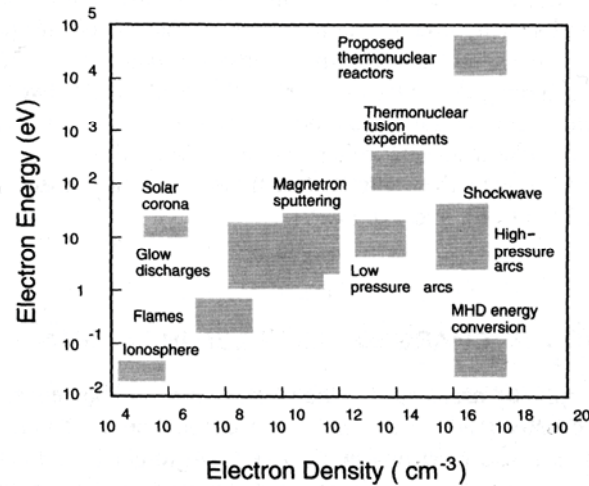


Figure 2.2: Plasma types by electron density and temperature [21]

Plasmas can be classified into three types [21]:

- in complete thermodynamic equilibrium (existing in stars during explosion)
- in local thermodynamic equilibrium (all temperatures are equal in each small volume of the plasma)
- not in local thermodynamic equilibrium – also named cold plasma (used for manufacturing purposes)

Several parameters characterise a plasma:

Plasma density

The density of the charged particles (electrons and ions) plays an important role in processing, because the reaction rates in the plasma depend on it. The concentration of electrons and ions is equal and much less than the density of neutral particles [23].

Plasma Temperature

The plasma temperature represents the mean translational energy of the different particles with varying masses and charges. Electrons receive their energy by the applied electric field which excites the plasma. Due to the fact that electrons collide with the other particles in the system, they lose part of their energy. The heavier ions dispense energy to the surroundings. Therefore, ions and electrons have different energies (temperatures). In cold plasmas, the energy of the electrons is the most important temperature, and is about 10^4 K. Since the temperature of the ions is much lower than that of the electrons at low pressures, the plasma is not very hot because the energy (heat) of the electrons transferred to the surroundings (neutrals, ions, container walls) is very small [21].

Degree of Ionisation

This parameter defines the multitude of charged particles in the plasma, especially the ions. The degree of ionisation for plasmas maintained in low - pressure discharges is about 10^{-6} to 10^{-3} [22].

Debye Length

If an electric field is created in the plasma, the charged particles move such that the influence of the field is diminished. This process is called Debye shielding. When an electric potential is applied between two surfaces in the plasma, the charged particles will move towards the surface of opposite charge. By doing so, these particles shield the surfaces from the plasma, which remains quasi-neutral. Therefore, the electric potential forms basically near the two surfaces over a certain distance λ_D , called Debye length [19, 23].

Plasma sheath

Two electrodes are inserted in the plasma and a potential is applied. At the negative electrode (cathode) electrons are very strongly repelled. Thus, in the vicinity of the surface the quasi neutrality can not be obtained. At the anode electrons are attracted so that there is a magnitude of positive ions too. These two ranges are called sheaths and they have a thickness of several Debye lengths. As a consequence, the potential of the plasma is positive relative to any surrounding surface [1]. A typical distribution is shown in Figure 2.3.

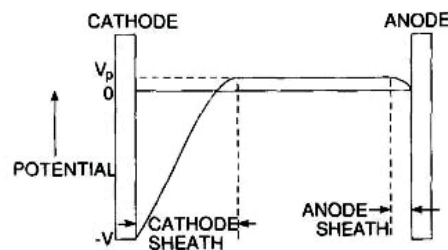


Figure 2.3: Voltage distribution across dc glow discharge [1]

Pressure

At low pressures ($p < 1$ Pa) the mean free path between two collisions is much higher than the thickness of the plasma sheet which is important for the rectilinear motion of ions [24].

2.2.1 Glow Discharge

Glow discharge is a kind of gas discharge which can be activated and sustained by direct current (DC), radio frequency (RF), or microwave power attached to a gas at low pressure. It creates a cold plasma without reaching the thermodynamic equilibrium.

Due to its importance for the present work, this chapter concentrates on DC glow discharges, which are excited by applying a DC voltage to two electrodes inserted in a gas at low pressure. As soon as a DC power is applied, a characteristic current-voltage curve develops (see Figure 2.4).

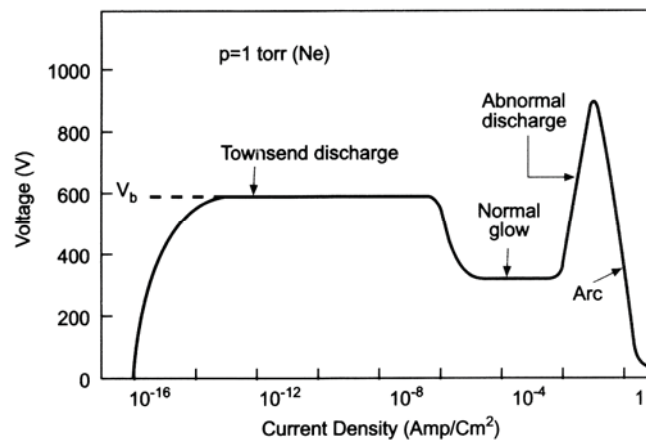


Figure 2.4: Characteristic current-voltage curve of a dc glow discharge [21]

At the beginning, a small current flows due to a few (natural) electrons in the gas. By increasing the voltage, more charged particles are created, consequently, ionising the gas. This charge multiplication causes a rise in current while the voltage remains constant - this is called Townsend discharge [1]. An avalanche process occurs, exciting a large numbers of electrons and ions. In the normal glow area, an equilibrium between the rate of formation of ions and the rate of their recombination with electrons is established. As a result, the gas starts to glow while the voltage drops and the current rises.

A further increase in power leads to the abnormal discharge region, where the current depends on the applied voltage [25]. This abnormal discharge region is the mode used for glow discharge processing. At higher current densities the cathode heats significantly to the point of thermionic electron emission, which is known as an arc [26].

The dominating processes in a plasma are the collisions of the electrons and all other particles. These collisions can be elastic or inelastic depending on the mass of the involved particles [1]. By the time the electrons have gained enough energy through the applied electric field, their most important function is to ionise the gas atoms and therewith sustain the plasma. The ionised gas collides with the surface of the cathode (target) and causes the emission of the target material which condenses on all present surfaces [27].

2.3 Sputtering

In recent years, the sputtering technique has been enormously developed as a result of downsizing micro-electronical devices. Many industries producing e.g. magnetic films for information storage, optical coatings or hard coatings for wear protection have benefited by this development [1].

This technology offers many possibilities like sputtering of metals or non-metals and reactive or non-reactive deposition. The procedure is always the same: Positive ions (mostly Ar^+) are generated using a plasma and accelerated through an applied electric field. If the ions hit the surface of the cathode with sufficient energy, target atoms are ejected by a momentum transfer. The sputtered atoms consist of 99% neutral particles which condense on the substrate and any other surface [27].

2.3.1 DC - Sputtering

Inside a vacuum chamber two electrodes are placed opposing each other. After evacuating the chamber, a working gas is led into until a partial pressure of about 10^{-2} mbar is reached. A negative voltage (some kV) is applied to the cathode (target material) while the anode is grounded. Because of the applied voltage, an abnormal glow discharge is ignited (see Figure 2.4). The processes taking place in the chamber are shown in Figure 2.5.

The pressure of the working gas plays an important role for the sputtered atoms. If the pressure is too high, the ejected atoms undergo too many collisions with gas atoms, consequently, they lose energy and are not efficiently deposited. On the other hand, if the pressure is too low, the glow discharge can not be sustained [1].

The technique described up to now is called diode sputtering and only works using conductive target materials. The deposition rates for hard coatings are very low [16].

Additionally, a negative potential can be applied to the anode/substrates, usually about -50 to -100 V. This potential is called bias voltage. Due to the applied voltage, some ions from the working gas are attracted to the substrate, resulting in an ion bombardment of the growing film [28] and in an improvement of the coating properties.

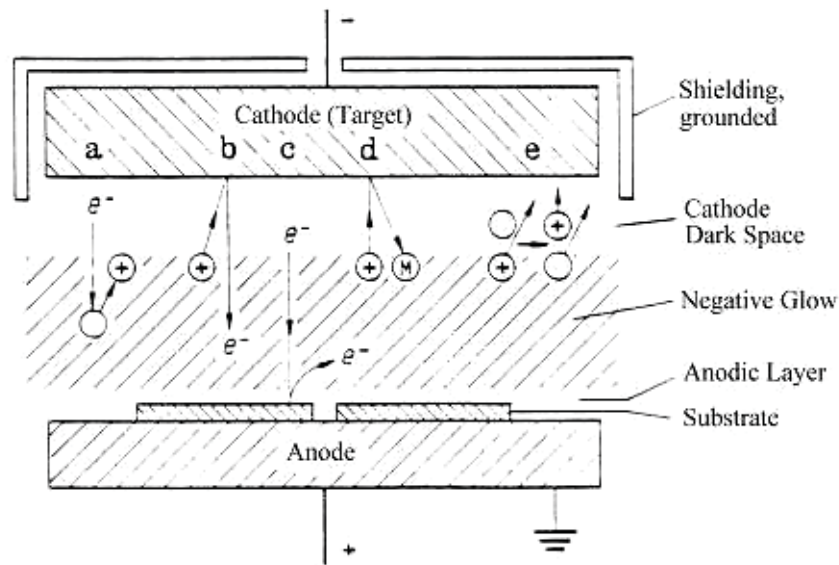


Figure 2.5: DC Diode Discharge: **a** ionisation, **b** electron emission from cathode, **c** electron emission from anode, **d** sputtering, **e** charge transition process [modified after 24]

2.3.2 Magnetron Sputtering

The low deposition rates of the sputtering process can be significantly increased by using magnetrons [21]. Hereby, a permanent magnet is positioned behind the cathode. The magnetron generates a magnetic field orthogonal to the cathode's electrical field, and in this way electrons get trapped and the plasma ionisation density increases near the target surface [29]. The electrons move on cycloid orbits (responsible for this behaviour is the Lorentz force), which results in higher erosion of the target. The disadvantage of this method is that the target is eroded very locally. Contrary, a benefit is due to the modified movement of the electrons as the substrate is not as thermally charged as without the magnetron [24, 27, 30].

There are three types of magnetrons: cylindrical, circular and rectangular. A typical planar circular magnetron is shown in Figure 2.6. The magnetic field lines are closed between the outer and the inner magnets and the magnets balance each other. Therefore this type is called **conventional balanced magnetron (CBM)** [28].

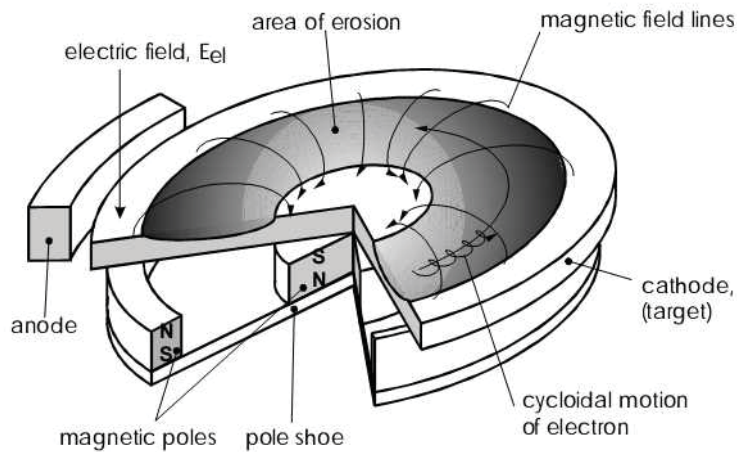


Figure 2.6: Balanced magnetron in planar configuration [28]

The other, even more important type of magnetrons is termed **unbalanced magnetron** (UBM). The decisive difference is that the magnetic field lines are not closed but partially opened towards the substrate. Thus, the probability of ionisation near the substrate rises and the amount of ions impinging the surface can be influenced.

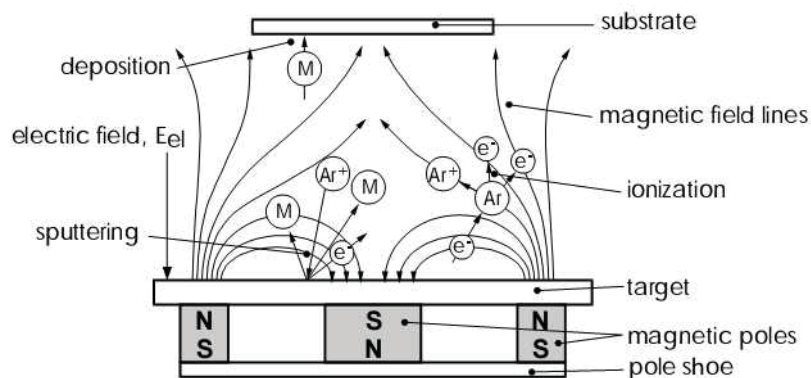


Figure 2.7: Unbalanced magnetron in planar configuration [28]

The bombardment of the substrate with energetic particles during film deposition can effectively influence the structural properties of the resulting film such as changes of crystal structure, orientation and grain size, modification of film stresses, and chemically improvement of the adhesion to the substrate and higher purity [31, 32].

2.3.3 Reactive Sputtering

The reactive sputtering technology is used for producing a thin film compound. For this purpose, metallic targets are sputtered in presence of a reactive gas typically mixed with an inert working gas (e.g. Ar). Preferred reactive gas species are oxygen, nitrogen and methane for compounds like Al_2O_3 , In_2O_3 , TiN, AlN, TiC, WC and SiC. The structure of the deposited film is a solid solution of target material mixed with the reactive element [1]. It is very important in practise to meet the precise stoichiometry of these films [33]. Therefore, it is necessary to adjust the partial pressure of the reactive gas very carefully because at the substrate surface the arrival rate of metal atoms has to be matched with the appropriate amount of reactive gas atoms to form the stoichiometric compound [34].

A constant material flux is maintained by sputtering a pure metal in argon atmosphere. Once a reactive gas is added to the chamber during sputtering it is able to react with the target, the substrates and the chamber walls. If there is enough reactive gas to form the compound, it is formed on both substrate and target. Since the sputtering rate for the compound on the target is much lower than that of the pure metal, this is called target poisoning. It is of great importance to balance the partial pressure of the reactive gas very accurately to obtain high sputtering rates.

2.4 Thin Film Growth

The properties of thin films are determined by their microstructure, which is defined by nucleation and growth, and are different compared to those of the corresponding bulk material, which is a unique characteristic of thin films. To design appropriate properties it is of special interest to influence the growth process.

2.4.1 Nucleation and Growth

Nucleation includes all processes which lead to a more or less continuous thin film on a substrate surface (Figure 2.8). The first step of nucleation is adsorption of an atom on the surface. The atoms impinge at the surface with a certain arrival rate and are either directly reflected or adsorbed. Atoms which dwell on the surface are able to diffuse or exchange their energy with other atoms or the lattice or desorb again. Due to the different chemical nature of the coating material and the substrate, deposition atoms can not immediately condense on the surface. Several "single" atoms form a cluster which is able to condense on the substrate [28]. These clusters are termed nuclei whereas the formation of clusters is called nucleation. Single adsorbed atoms diffuse on the surface and attach to existing clusters. This process is called growth. During deposition, formation and growth of clusters happen at the same time.

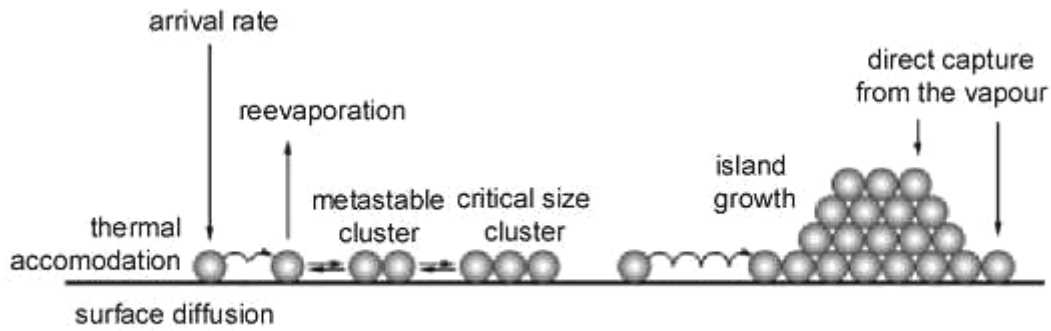


Figure 2.8: Schematic of nucleation and growth processes [28]

There are three types of crystal growth on surfaces as shown in Figure 2.9 [35]. The first mode is termed layer growth or Frank-van der Merwe mode (Figure 2.9-a) and it is characterised by atoms which are strongly bound to the surface and therefore form a complete monolayer. In Figure 2.9-b the opposite behaviour is displayed: Small clusters nucleate directly on the surface and grow into islands of condensed phase. This is also called Volmer-Weber mode. There is also an intermediate mode called Stranski-Krastanov mode or layer + island growth. In this case first a few monolayers are formed followed by island growth onto them. A possible explanation for this appearance is that the lattice parameter of the layer can not be continued into the bulk deposit [36]. The affinity of the film material to the substrate, the activation energy of diffusion and the binding energies between film-film and film-substrate determine ultimately which type of crystal growth occurs [37]. For example, when the atom-atom binding is stronger than the atom-substrate binding, then island growth occurs. Frank-van der Merwe growth occurs when the atom-atom binding is equal or less strong than the one between atom and substrate.

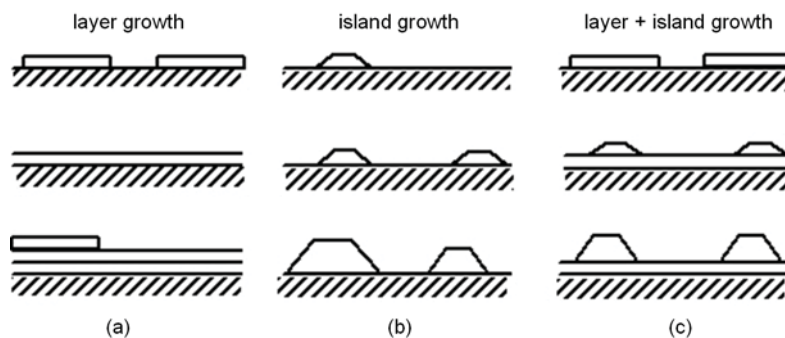


Figure 2.9: Schematic of three modes of film growth on substrates: **a** layer growth, **b** island growth, **c** layer and island growth [36]

The contact and coalescence of two or more layers/islands is important to form a continuous film. Distinct islands are orientated differently. The unique attribute of coalescence is that islands with the lowest energy per atom consume the others [13]. "Consumed atoms" readjust their position by bulk diffusion.

2.4.2 Structure Zone Models

Thin films are usually deposited far away from thermodynamically equilibrium. Therefore, it is of great interest how process parameters influence the structure and furthermore the related coating properties [38, 39]. Structure zone models (SZM) based on phenomenological observations have first been established by Movchan and Demchishin [40]. As show in Figure 2.10 the microstructure of a deposited film depends on the ratio of substrate temperature (T_s) to the melting point (T_m) of the coating material. This ratio, the homologous temperature, determines the incidence condensation, surface or bulk diffusion and recrystallisation, resulting in certain structures and properties in each zone which denotes that only thermally induced mobility is considered [41].

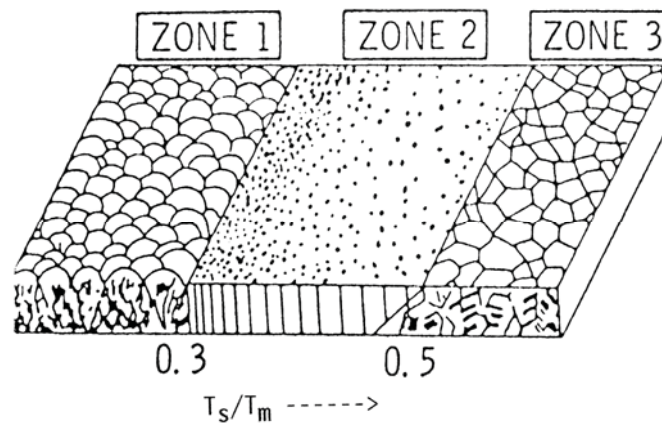


Figure 2.10: Diagram of structure zones for film growth during evaporation [40]

Zone 1: Due to the low substrate temperature, the mobility of the adatoms is low, hence, shadowing effects take place. The layer is characterised by free standing crystals with a porous structure and high inner tension.

Zone 2: A smooth coating is formed with a dense columnar structure as a result of higher diffusion.

Zone 3: Bulk diffusion processes such as recrystallisation take place during deposition and a coarse grain structure is observed [42, 43].

This simple model has been extended by Thornton [42] for different working gas pressures and by Messier et al. [41] for different ion energies (see Figure 2.11). With increasing working gas pressure, the structure zones are shifted to higher temperatures due to a reduction in surface mobility of adatoms by adsorbed impurities. Thornton also found a new zone – the transition zone T – characterised by a fibrous, dense packed grain structure. The modification of the SZM by Messier et al. [41] considers the negative bias voltage which enhances the mobility of the impinging atoms due to their higher energy. The ion bombardment affects the density, grain size, stress state, and growth morphology of the film [38].

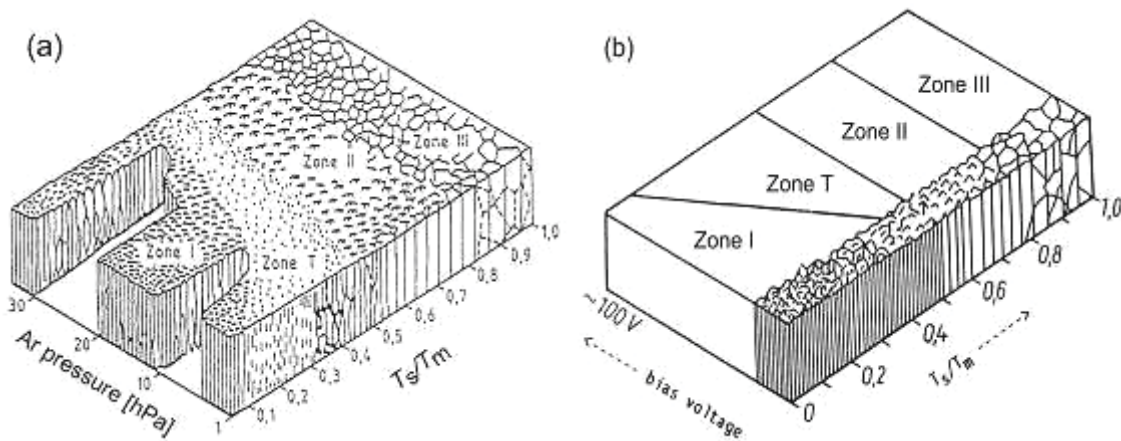


Figure 2.11: Modified structure zone models after **a** Thornton [42] and **b** Messier et al. [41]

Generally, thin films grow from single nuclei and the higher the ion bombardment present the more nuclei emerge. Substrate temperature, pressure and the angle of incidence affect growth and morphology of the coating. Each crystal grows in direction of the ion flux and under various conditions, different kinds of coating structures develop as shown in Figure 2.12.

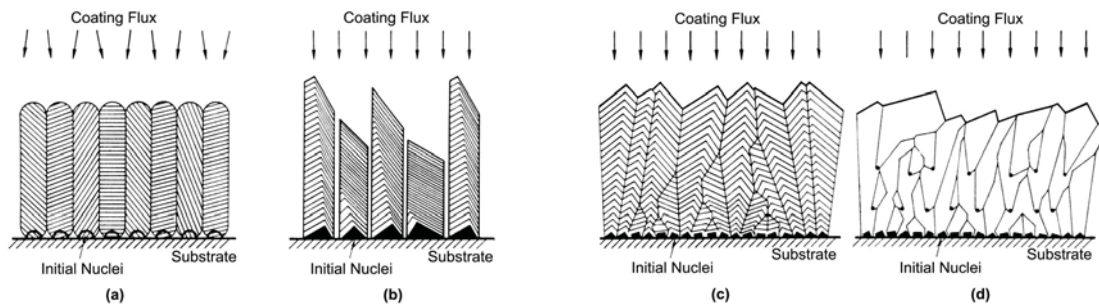


Figure 2.12: Structure development under various conditions [42]

In case **a**, with low temperature, there is almost no adatom surface mobility. The direction of the ion flux slightly varies and therefore, spherical nuclei grow to a dense columnar structure. In Figure 2.12-**b** parallel flow and low temperature lead to free standing single crystallites. The structure of the coating is porous and the surface shows high roughness. When the temperature is increased, diffusion is possible and a dense and smooth film is formed (Figure 2.12-**c**). If repeated nucleation occurs, a structure as shown in Figure 2.12-**d** can be observed [36].

Moreover, structure evolution also depends on incorporated impurities and intentionally introduced additives which plays an important role for polycrystalline coatings. These impurities or additives state a second sort of atoms, and additionally to the parameters mentioned above, have a drastic influence on the structure zones as shown in Figure 2.13. Impurities exert strong influence on real SZM as they are incorporated in the growing film and constitute further nucleation sites. For low temperatures (Zone I), the nucleation density is very high and due to the very low surface mobility adatoms stick where they fall. Since coalescence does not occur, grain growth is inhibited and thus, a very fine structure, also called nanocrystalline, especially for high impurity contents, can develop (Figure 2.13-**d**) [44].

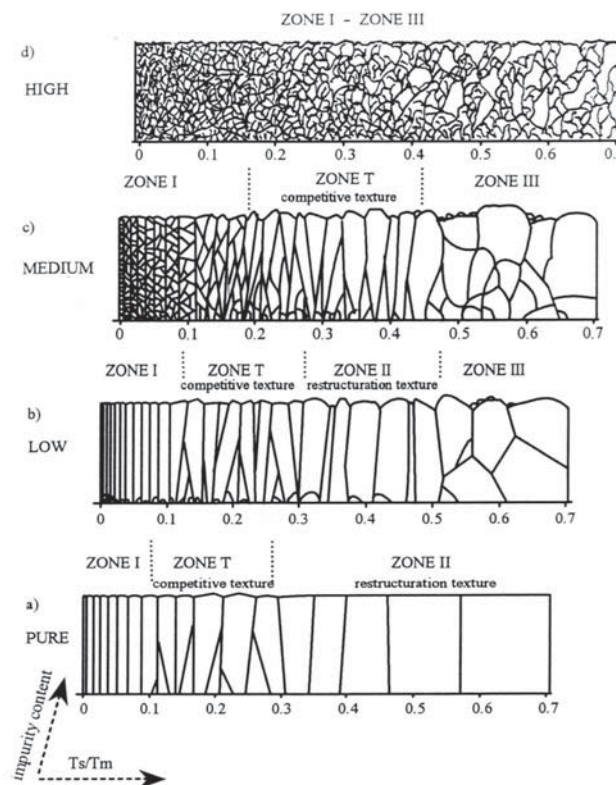


Figure 2.13: SZM of **a** an ideal structure and **b - d** real models with low to high impurity concentrations [44]

3 Hardening Mechanisms

Every material resists plastic deformation differently, some deform easily others can withstand high external mechanical loads. Responsible for this specific material behaviour is the movement of dislocations. Hardness increases the more dislocations are hindered in their motion. This means that higher stresses are necessary to deform the material. Well known hardening mechanisms are [45]:

- Strain hardening
- Solid solution hardening
- Precipitation hardening
- Hall-Petch and size effects

Strain Hardening

Ductile metals become harder during plastic deformation at low temperatures. The reason for this behaviour is the interaction between dislocations and their strain fields. Furthermore, new dislocations are generated resulting in an increased dislocation density. Moving dislocations interact with the strain fields of others and are either attracted or repulsed. The higher the dislocation density is, the more likely is the mutual repulsion. Due to this interference, higher stresses are required to deform the metal [45].

Solid Solution Hardening

In general, an alloy is harder than the pure material because the alloying atoms normally induce lattice strain [45]. These strains interact with the dislocations and consequently, the motion of dislocations is restricted.

There are two possible arrangements for the alloying atoms in the solid solution, either on interstitial or on substitutional positions.

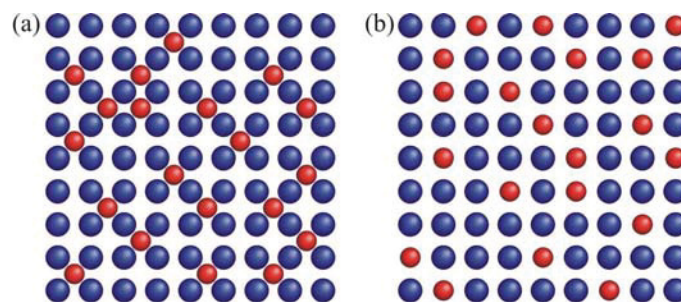


Figure 3.1: **a** interstitial positions and **b** places on lattice sites of foreign atoms [46]

Precipitation Hardening

Small particles, which are either added during production (called dispersoids) or formed during heat treatment, represent effective obstacles to dislocation movement [47]. There are three shapes of precipitates as shown in Figure 3.2: **a** coherent, **b** semi-coherent and **c** incoherent.

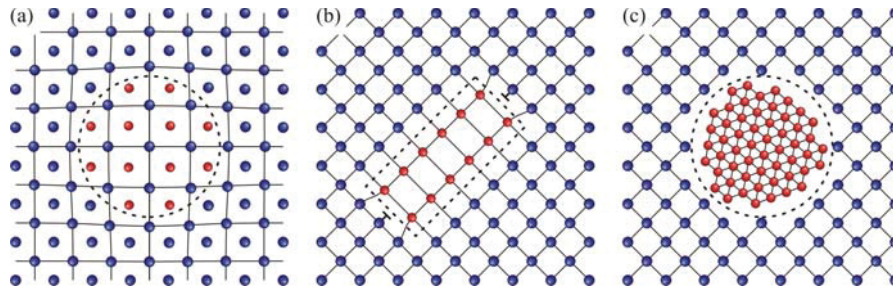


Figure 3.2: Precipitates distinguished by their relation to the lattice [46]

Particles which segregate incoherently from the matrix show the same behaviour as dispersoids. Dislocations have to bypass them. Coherent and semi-coherent precipitates are only cut by dislocations which are on the same slip plane. The mechanism which occurs depends on the size of the particles as shown in Figure 3.3. The increase in strength arises from the energy needed to move dislocations forward. Small particles can be easily cut and big particles simply bypassed. At a certain particle size at the transition from cutting to bypassing, a maximum in strength is observed [48].

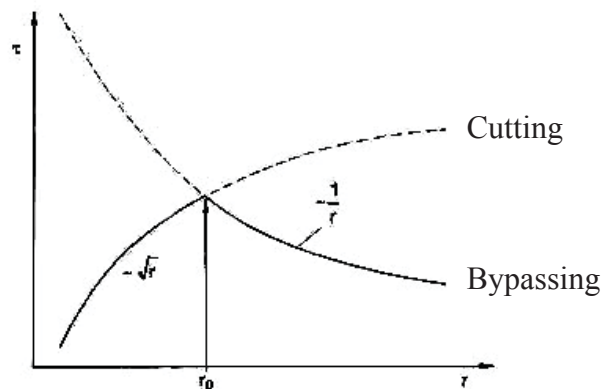


Figure 3.3: Increase in strength depending on particle size and way of interaction with dislocations [48]

3.1 Strengthening by Grain Size Reduction and Size Effects

Grain boundaries represent an obstacle for the sliding of dislocations as shown in Figure 3.4. Plastic deformation is characterised by the motion of dislocations and the formation of slip bands. When a dislocation comes to a grain boundary, it is normally not possible that it moves on the same slip plane into the other grain since grains are usually orientated differently. Consequently, dislocations pile up at the grain boundary. This gives rise to a stress concentration that triggers off new dislocation sources in the adjacent grain [49].

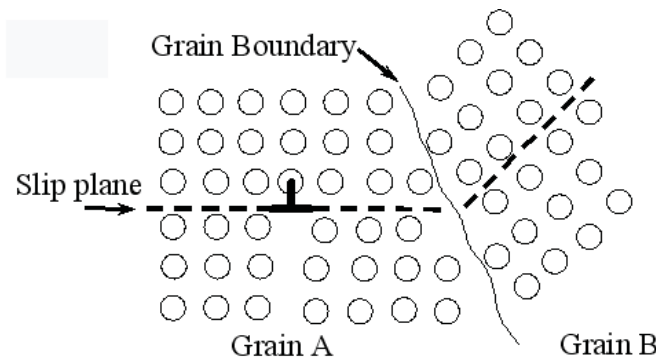


Figure 3.4: Motion of a dislocation as it encounters a grain boundary [45]

The required stress can be expressed by the Hall – Petch relationship:

$$\sigma_y = \sigma_0 + k \cdot d^{-\frac{1}{2}} \quad \text{Equation 3.1}$$

σ_y ... yield strength, σ_0 ... lattice friction stress,
 k ... constant, d ... average grain diameter

In small grains fewer dislocations can pile up, and therefore, more energy is needed to induce a dislocation source in the next grain. This mechanism can not be applied for any grain size. At least one dislocation loop must fit into the grain (see Figure 3.5-**a** and **-b**). Therefore, for very small grains (<10 nm) this mechanism does not work and the strength decreases with decreasing grain size as depicted in Figure 3.5-**c** [50, 51].

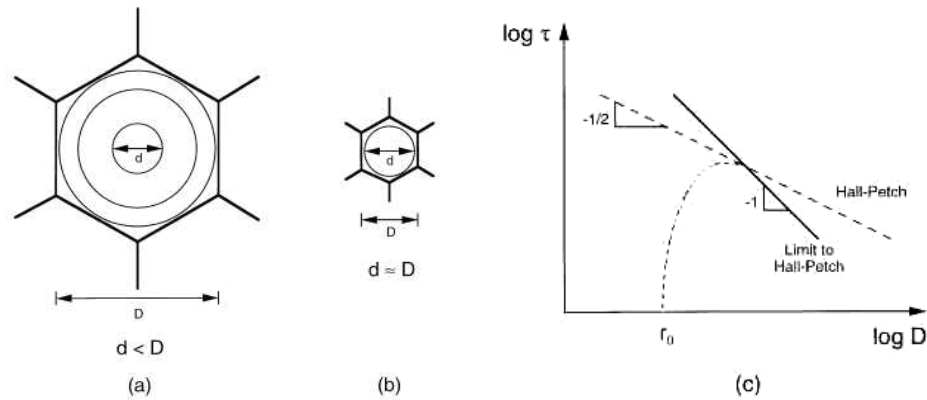


Figure 3.5: **a** dislocation loops in one grain, **b** minimum size for valid Hall - Petch equation, **c** inverse behaviour left to the intersection of the dotted and the heavy line [50]

For nanocrystalline materials, which have by convention a grain diameter smaller than 100 nm, the plastic behaviour is not fully understood. Hardening still occurs even after reducing grain sizes of metals below 100 nm, but at a reduced slope. For ultra-fine grain sizes (< 20 nm) an inverse Hall-Petch effect can be observed. Grain boundary sliding, creep diffusion, triple junctions and impurities are supposed to be the reason for this behaviour. Ceramics with grains at nanoscale often exhibit better mechanical properties than their coarser-grained samples, like improved ductility at room temperature and at elevated temperatures significant compressive ductility and strain rate sensitivities [52, 53, 54].

Deformation at a nanoscale does not only take place by dislocation movement, which is diminishing the smaller the grains are, but also by grain boundary sliding. This mechanism and short range diffusion, both enabled by an increase of the grain boundary fraction, are the dominating deformation mechanisms for conventionally brittle materials in their nanophase forms [55].

There are different possibilities for the structural composition of nanostructured materials. Gleiter classified nanostructured materials with respect to their chemical composition and the dimensionality of the crystallites as illustrated in Figure 3.6. The categories which define the shape of the crystallites are: layer-shaped, rod-shaped and equiaxed crystallites. The possible differences in chemical composition are divided into families. The first family consists of crystallites and interfacial regions which all have the same chemical composition. Different chemical compositions for crystallites characterise the second family, and the third family is obtained when the composition variation occurs between crystallite and interfacial regions. The fourth family is represented by nanometer-sized crystallites dispersed in a chemically different matrix [54, 56].

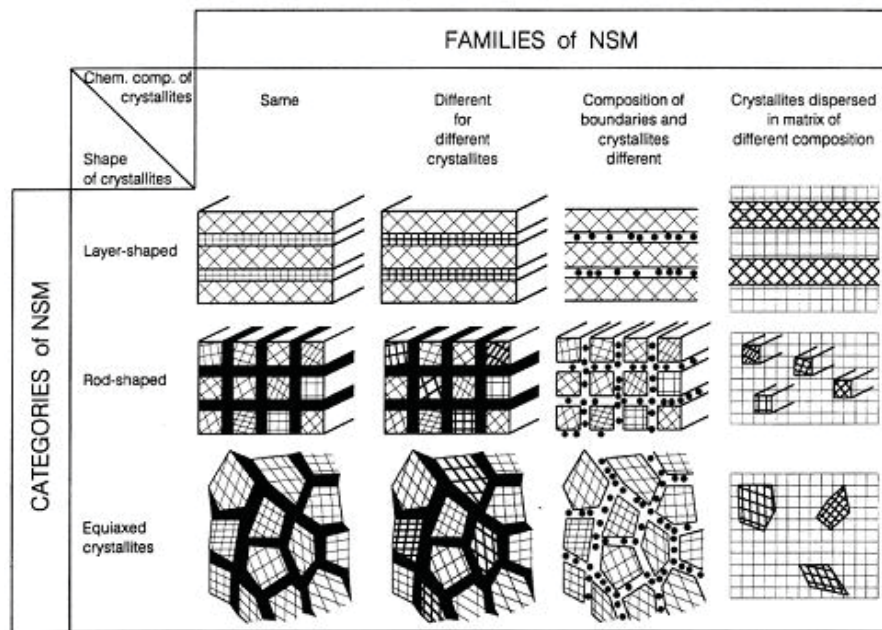


Figure 3.6: Classification scheme for nanostructured materials according to their chemical composition (family) and the dimensionality (shape) of the crystallites/structural elements (categories) [56]

For hard nanocomposite coatings, which belong to the families two and three, Patscheider et al. [57] proposed a specific zone model for different fractions of nanocrystalline (TiN) and amorphous phases (Si_3N_4) (see Figure 3.7.-a). The achieved hardness depends strongly on the morphology of the coating as illustrated in Figure 3.7.-b. Si_3N_4 free titanium nitride forms large elongated crystallites (~ 100 nm). Even small amounts of silicon nitride Si (0 – 3 at.% in zone A) hinder TiN in further growth and encapsulate it with a monolayer (at 3-4at.% Si). This change in structure causes the increase of hardness in zone A. Zone B (Si = 3 – 10 at.%) is characterised by TiN grains with average size between 5 – 10 nm. The amorphous Si_3N_4 completely covers the TiN crystallites when the Si content is raised to 10 at.% Si. This thin layer of silicon nitride (~ 0.4 nm), which separates the TiN grains, is sufficient to promote the hardness of the composite. The fully interpenetration of the two phases is reached at about 10 at.% Si and this is called percolation threshold. In zone C the percolation threshold is reached and the mean grain separation exceeds a certain value (~ 0.5 nm, in this case). So, when Si content is raised above 10 at.% a remarkable hardness loss occurs and the hardness of the nanocomposite is more and more determined by the amorphous phase [57].

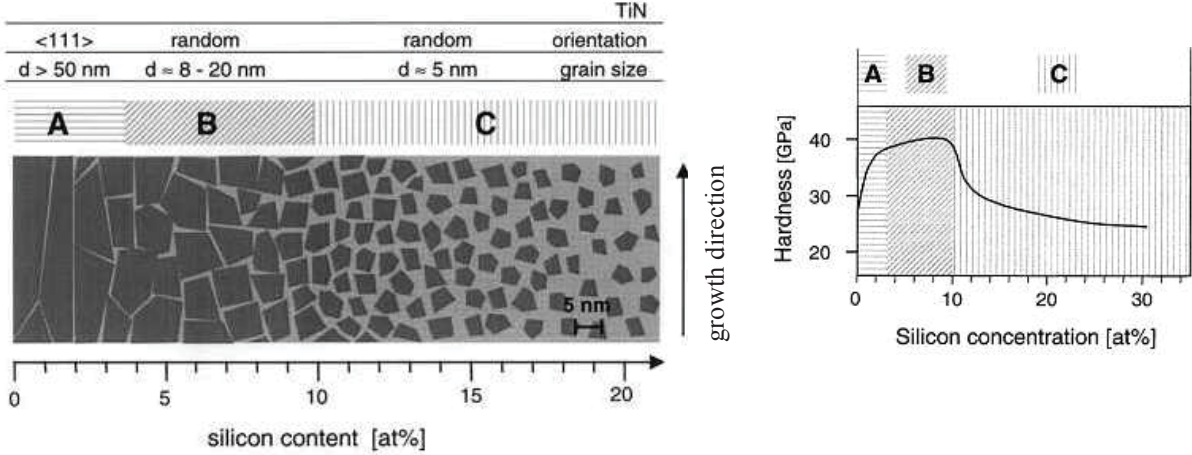


Figure 3.7: a morphological zone model (dark areas represent nanocrystals, brighter areas-amorphous phase)
b three zones of different hardness [57]

4 Thermally Activated Processes

Processes which run easier at higher temperatures are called thermally activated processes. Many of them depend on temperature with $\exp(-Q/kT)$, the Boltzmann coefficient [48]. In this expression Q is the activation energy, which is related to the concerned process, T is the temperature and k the Boltzmann constant.

In materials especially the vibrations and movements of atoms are enforced and facilitated at elevated temperatures. Many processes like diffusion, recovery, and recrystallisation depend on the motion of atoms and vacancies.

4.1 Diffusion

Diffusion in solids denotes the motion of atoms within a lattice due to temperature. There are two possible types of diffusion, either self diffusion occurs in pure metal or a homogeneous alloy, or diffusion takes place to equalise differences in the concentration of one alloy constituent. In both cases mass transport occurs. For a single atom to meander stepwise through the lattice, two requirements have to be fulfilled [45]:

- There must be an empty adjacent site.
- The atom has to have enough energy to break bonds with its neighbours (which is more difficult at lower temperatures).

There are several mechanisms for atom migration but the two most common are interstitial and vacancy diffusion, as shown in Figure 4.1. Interstitial diffusion mainly occurs when the migrating atom is very small such as H, C, N and O. These atoms are not placed in the crystal lattice but in interstitial positions, and they can just move into another interstitial position. This diffusion mechanism is not defect controlled (see Figure 4.1-a) [49].

The second form of diffusion –vacancy diffusion– needs vacant lattice sites for the migration of atoms (Figure 4.1-b). For this type of diffusion it is important to mention that coatings produced by PVD-processes exhibit a high defect density because of the ion bombardment during growth [58].

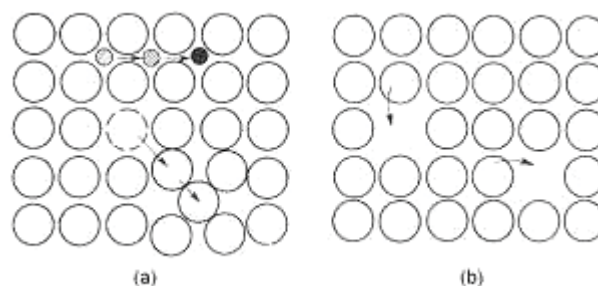


Figure 4.1: Illustration of **a** interstitial diffusion and **b** vacancy diffusion (modified after [59])

4.2 Recovery and Recrystallisation

Metals work-harden during deformation due to a significant increase in the dislocation density. In Figure 4.2-**a** and -**b** the differences before and after deformation are shown. This status will remain at low temperatures as the driving force for atom migration is too low. If the temperature is increased, the thermal energy is high enough to initiate dislocation gliding, climbing, and cross slipping, and dislocations move to reduce the large strain energy of the lattice. Previously, as soon as the temperature delivers enough energy, healing of point defects takes place. Moreover, vacancies which move easily cause dislocation climbing. Figure 4.2-**c** represents schematically a recovered microstructure after annealing, where dislocations rearranged due to their tension fields to reduce strain energy, but large-angle boundaries are unaffected [49, 60].

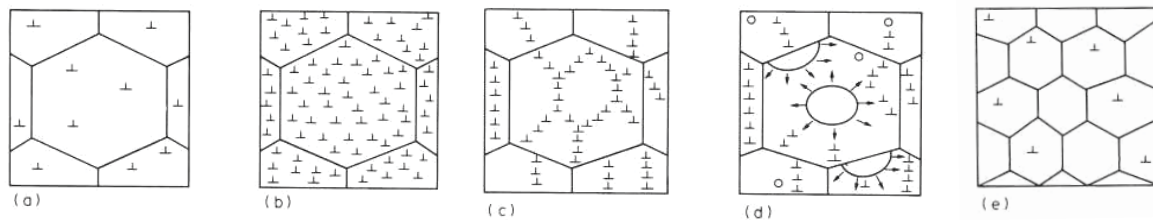


Figure 4.2: Changes in microstructure due to thermal induced processes: **a** not deformed, **b** after plastic deformation, **c** recovery, **d** recrystallisation, **e** final grain [60]

Besides recovery, recrystallisation may also occur during heat treatment. In this case, the microstructure is completely replaced by a new unstrained one [49]. As shown in Figure 4.2-**d**, this process runs by nucleation and growth of new grains until the whole lattice consists of undeformed grains (Figure 4.2-**e**). Furthermore, it is important to mention that, contrary to recovery, recrystallisation depends on incubation time [49].

The driving force for primary recrystallisation is the stored dislocation energy. After new small grains are formed, another recrystallisation process can take place in order to diminish interfacial energy which results in grain coarsening.

4.3 Thermally activated processes in PVD Coatings

PVD coatings with a nanocrystalline structure exhibit high defect densities due to ion bombardment during deposition. As discussed previously, the grains are too small to contain many dislocations, and the defect density comprises mainly point defects. Thermally activated processes during annealing in nanostructured PVD coatings are thus based in healing of zero dimensional defects. This annihilation process leads to relaxation of intrinsic stresses. Investigations have shown that after annealing of point defects, nucleation of new grains does not occur due to the low mobility of dislocations (even at elevated temperatures). Similar to weakly deformed metals, it is much more likely that only grain coarsening happens as there is much interfacial energy stored in the material due to the many grain boundaries [48, 61].

5 Residual Stresses

Thin films which are grown under non-equilibrium conditions on a substrate often show high residual stresses. In case that these films could be detached from the substrate, the residual stresses would cause a bending of the film [62].

Generally, there is a distinction between intrinsic or growth stresses, which are introduced during deposition, and extrinsic stresses, which arise from external influences, for example different thermal expansion coefficients of substrate and coating or creep/plastic deformation [63]. Growth stresses actually depend on the materials involved, the substrate temperature during deposition, and the growth flux. Mechanisms for intrinsic stress generation during deposition are [64]:

- Structural damage as a result of ion bombardment
- Grain growth
- Vacancy annihilation
- Incorporation of impurities

Unfortunately, the understanding of growth stresses and their origins is not well developed. Generally, sputtered films prepared at high pressures have tensile stresses whereas the bombardment with energetic particles during low-pressure sputter deposition gives rise to high compressive film stresses [64].

5.1 Growth Stresses in Polycrystalline Films

For many film-substrate material combinations growth occurs after the Volmer-Weber mechanism. Typical for this growth mechanism is that deposited material first forms discrete islands on the substrate surface. After the initial nucleation, subsequent stages of growth include island growth, island-to-island contact and coalescence into larger islands, large area contiguity and filling in of the remaining gaps to form a cohesive film [64].

During steady deposition, many materials show a similar stress evolution as indicated in Figure 5.1. First the stress becomes compressive, then tensile and then compressive again. The generation of initial compressive stress is usually attributed to surface and/or interface stresses and is active from the onset of growth until the islands coalesce. The incremental stress tends to become tensile when mutual contact of islands occurs due to the closing of small gaps between adjacent grains by forming grain boundaries. For high mobility materials the average stress decreases until it becomes compressive again. Probably, the compressive stress that arises in polycrystalline films is due to excess atoms comprising the film [64].

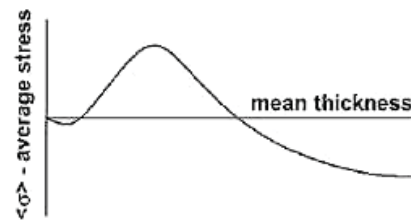


Figure 5.1: Schematic representation of film stress versus mean film thickness during growth [64]

One possible mechanism for generating compressive stresses by incorporating excess atoms in films with high-mobility materials, such as Cu, is shown in Figure 5.2. Two compressive ledges at the surface can create enough room to incorporate an extra atom [65].

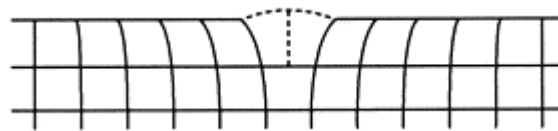


Figure 5.2: Adjacent ledges allow the incorporation of an extra atom [65]

Moreover, for sputtering processes compressive growth stresses are especially influenced by the bombardment of the surface by energetic particles. It has been observed that the amount of damage induced at the surface due to the bombardment depends on the energy of the arriving atoms and the background pressure of the inert gas. Low pressures and low deposition rates lead to the evolution of compressive stresses, whereas high pressure leads to tensile stresses in the film [63, 64].

5.2 Substrate Curvature

As discussed above, stresses in thin films have multifaceted origins. These macroscopic residual stresses (σ_{res}) consist of an intrinsic part (σ_{int}) and an extrinsic part (σ_{ex}) displayed in Equation 5.1. If thin films are attached to a flexible not too thick substrate, bending of the substrate is induced due to the high residual stresses. Intrinsic stresses are also called growth stresses and have been discussed in chapter 5.1. Extrinsic (also called thermal, σ_{th}) stresses derive from different thermal expansion coefficients of the coating and the substrate material and therefore vary with temperature [66].

$$\sigma_{res} = \sigma_{int} + \sigma_{th}$$

Equation 5.1

After deposition, when the coating-substrate composite cools down from deposition temperature, thermal stresses increase according to [67]:

$$\sigma_{th} = -\frac{E_C}{1-\nu_C} \cdot (\alpha_C - \alpha_S) \cdot (T_C - T_0) \quad \text{Equation 5.2}$$

In this equation α represents the thermal expansion coefficient of the coating C and the substrate S, and T the temperatures of the coating and surroundings (E is the Young's modulus, ν Poisson ratio, both of the coating).

Residual stresses can be measured by determining the curvature of the sample (see Figure 5.3). The characteristic values are: l_x and l_y represent length and width of the specimen, t_s and t_c thickness of substrate and coating respectively. σ_{xx} , σ_{yy} , σ_{zz} are the stress components in all three spatial directions. For this arrangement (coating on top) tensile stresses lead to an upward bending and compressive stresses to a downward one as shown in Figure 5.3.

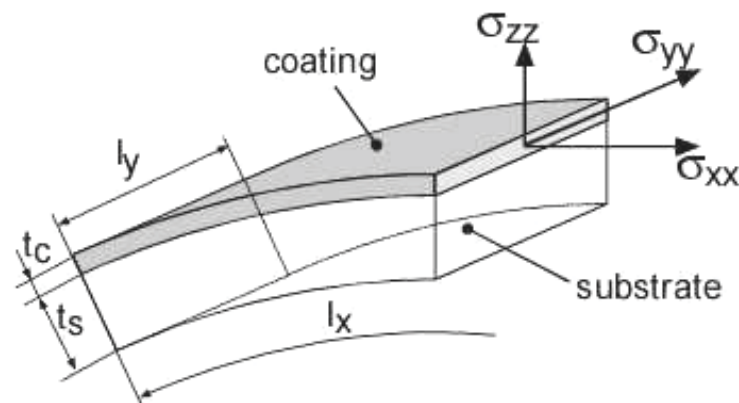


Figure 5.3: Schematic representation of a bended coating-substrate composite caused by residual compressive stresses [28]

If the sample is coated only on one side and the film is thin compared with the substrate ($t_c \ll t_s$), the normal stress σ_{zz} can be neglected. For the plate geometry the sample should expose a biaxial stress state. The residual biaxial stress can be calculated with the modified Stoney formula [68]:

$$\sigma = \frac{1}{6} \cdot \left[\frac{E_S}{1-\nu_S} \right] \cdot \frac{t_s^2}{t_c} \cdot \frac{1}{R} \quad \text{Equation 5.3}$$

This formula expresses the strain by stress and elastic properties by relating the curvature of the coating-substrate composite to the residual stress in the thin coating. The ratio of $1/R$ is the curvature and σ denotes the biaxial stress. This equation is valid if the $1/R \gg t_s$ and $l_y < l_x/2$ are given.

6 Tribological Properties

Tribology is a multi-disciplinary science that combines the topics friction, wear and lubrication. It can be defined as the science and technology of interacting surfaces in relative motion and the practices related thereto [69].

Nowadays, there is a growing need to minimise or control friction and wear e.g. to extend lifetime of machinery, to make engines more efficient, to improve safety, and of particular importance to save energy. In recent years it has become common to utilise surface treatments and coatings to influence friction and wear [70].

Friction and wear are not material properties but they are attributes of the engineering system – also called tribosystem. Some of the elements of such a system are displayed in Figure 6.1. Here, the system consists of two materials (M_1 , M_2) in a specific atmosphere and involved elements such as velocity (u), normal load (F) and environmental parameters like temperature (T) or lubricants [70].

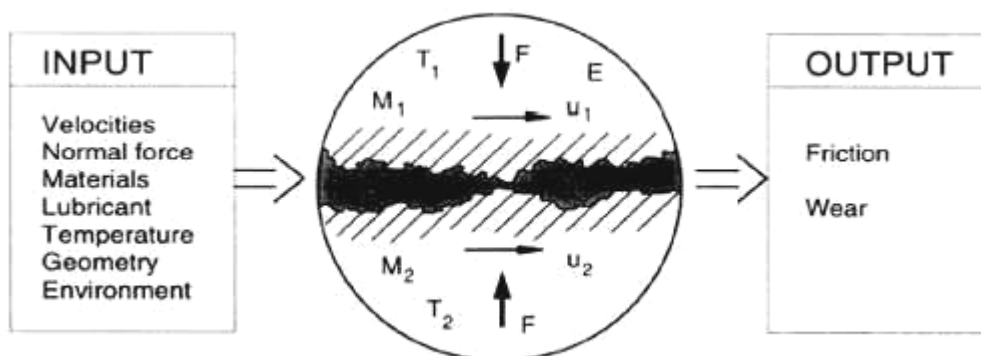


Figure 6.1: Illustration of a tribosystem showing material, contact condition and environmental parameters influencing the tribo-physical/-chemical contact processes that control friction and wear [70].

Friction is defined as tangential resistance to motion and evolves from interactions of solid bodies moving relatively to each other. Friction is characterised by the coefficient of friction, μ , which denotes the quotient of the frictional force F divided by the normal load w on the contact [70]:

$$\mu = \frac{F}{w} \quad \text{Equation 6.1}$$

Wear can be defined as: "Progressive loss of material from the surface of a solid body due to mechanical action". For design and material purposes it is important to quantify wear and have a classification number that allows the comparison of different materials. For this purpose, the wear rate K has been formulated. K is directly proportional to V , the worn volume, and inversely proportional to w , the normal load, and s , the distance of movement [70, 71, 72]:

$$K = \frac{V}{w \cdot s} \quad \text{Equation 6.2}$$

6.1 Friction

The mechanism of friction was first explained by the adhesion between surface asperities. This concept was developed by Bowden and Tabor (1950), who stated that when two asperities are forced into contact they will weld together due to adhesion. They also included a ploughing effect into their concept.

A new theory of friction was proposed by Suh and Sin (1981), who showed that the mechanical properties affect the frictional behaviour. They identify three basic mechanisms as the origin of friction (see Figure 6.2) [70]:

- Adhesion
- Ploughing
- Asperity Deformation

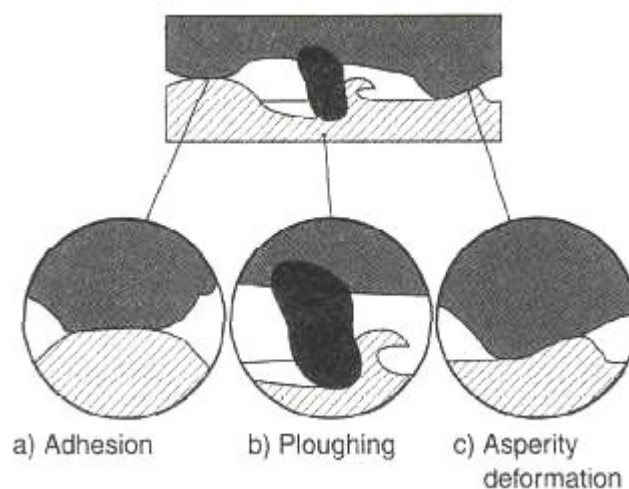


Figure 6.2: Three components of friction: **a** adhesion, **b** ploughing, **c** asperity deformation [70]

Adhesion

When two "flat" surfaces are placed in contact under load, contact takes place at the tips of asperities. At the regions of true contact, atoms of one surface may bind to those of the other and form junctions. For metals, this is referred to as cold welding. When sliding occurs, these junctions have to be sheared. Therefore, additional force is necessary to move these two surfaces [73].

Ploughing

In the case that one surface is harder than the other, surface asperities plough grooves into the softer material. This can also occur when hard particles are trapped between two surfaces. The energy necessary to deform the material is the origin of friction. Generally, ploughing leads to macroscopic deformation, with the dimensions of the resulting groove being orders of magnitude greater than the asperities of the surfaces [72].

Asperity Deformation

Resistance to motion rises also from plastic deformation of asperities as they slide over each other [70].

6.2 Wear

The removal of material from the surface can be described by four main mechanisms which are illustrated in

Figure 6.3 [71]:

- Adhesive Wear
- Abrasive Wear
- Surface Fatigue
- Tribochemical Reaction

Adhesive Wear

High local pressure between contacting asperities leads to plastic deformation and adhesion and results in the formation of local junctions. When the force necessary to break the junction across the original interface during sliding is larger than that to break through some surface inside the material then the break will occur through the latter surface, and material is transferred from one surface to the other (see Figure 6.3-a) [71].

Abrasive Wear

The displacement of material caused by the presence of hard particles or hard surface protuberances is called abrasive wear (see Figure 6.3-b). There are two possible mechanisms: plastic deformation (no wear particles are formed) or fracture with limited plastic deformation (wear debris is formed). Abrasive wear can be classified into two-body and three-body abrasion. When the abrasive can move freely between the contacting surfaces, it is called three-body abrasion. In two-body abrasion, surface protuberances or hard particles which are attached to one of the contacting surfaces act as abrasive [72].

Surface Fatigue

Materials which are exposed to repeated loading and unloading cycles may form subsurface or surface cracks. The typical pattern of the damage is pitting: the breakup of the surface with the formation of large fragments, leaving large pits in the surface (illustrated in Figure 6.3-c) [71].

Tribochemical Reaction

When the relative motion of surfaces takes place in a corrosive environment, the surfaces can react with the medium, which can be gaseous or liquid. The most common reactive species is oxygen provided by air. Oxidation takes place on almost every surface. The wear proceeds by continual removal and new formation of reaction layers on the surfaces (see Figure 6.3-d). Thus, tribochemical wear needs both corrosion and relative motion [72].

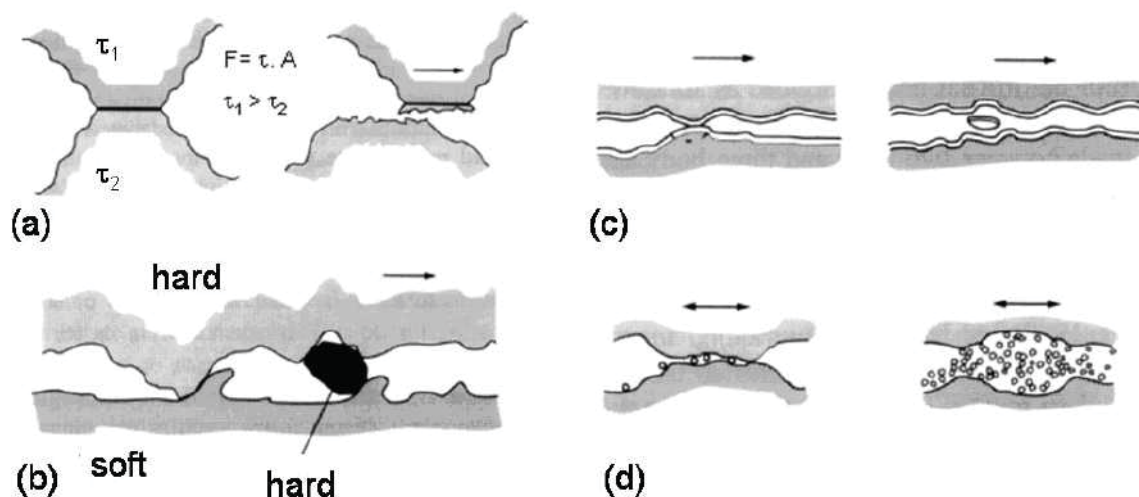


Figure 6.3: Schematic description of the wear mechanisms: **a** adhesive wear, **b** abrasive wear, **c** surface fatigue, **d** tribochemical reaction [70]

7 Experimental

7.1 Coating Deposition

7.1.1 Coating Facility

The coatings investigated in this work were deposited in a laboratory scale unbalanced DC magnetron sputtering system (shown in Figure 7.1) using Ar as working and N as reactive gas. This system consists of a cylindrical vacuum chamber (\varnothing 380 mm x 235 mm), an AJA magnetron cluster (3 magnetrons with 2" targets), a sample holder (with adjustable rotation speed), the power supply for the magnetrons and vacuum and gas inlet systems.

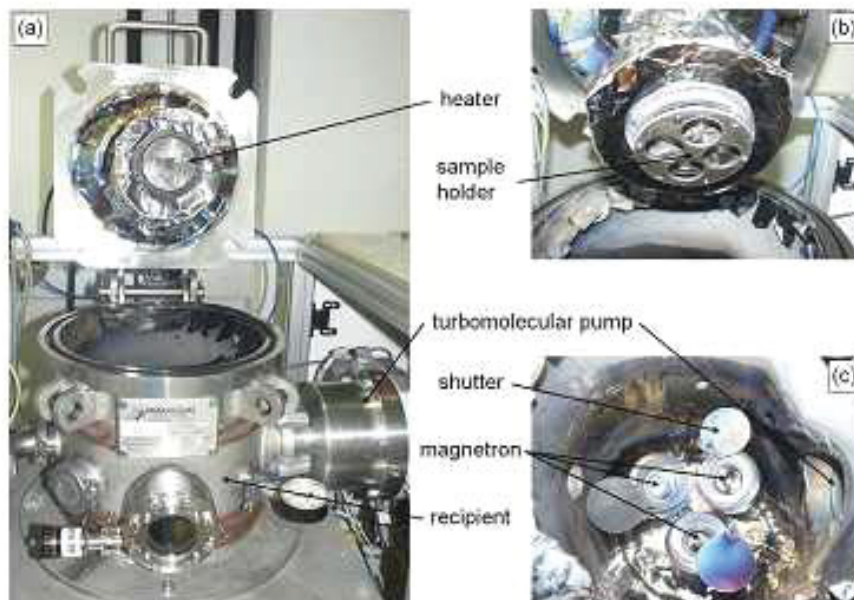


Figure 7.1: **a** Laboratory scale high-vacuum sputtering system, **b** rotating sample holder, **c** three magnetron cluster flange [61]

Two bipolar pulsed DC power supplies (ENI RPG-50, programmable frequency 50-250 kHz, duty cycle from 2.5 to 40%) are used as magnetron power supply for three targets, whereas one serves two (Ti) targets simultaneously. These ENI power supplies can be operated in DC and pulsed DC mode. A third pulsed DC power supply (ENI RPG-50) was used for plasma etching of the substrates prior to coating deposition and to apply a negative bias voltage during deposition.

A dual stage rotary vane pump (Pfeiffer Vacuum Duo 20, pumping speed 24m³/h N₂) and a turbomolecular pump (Pfeiffer Vacuum TMH 521 P, pumping speed 300 l/s N₂) are used for high-vacuum generation.

Three water-cooled targets (∅ 50.4 mm), which can be closed by a shutter (Figure 7.1-c), are mounted on the magnetrons in the lower part of the vacuum chamber. At the lock of the chamber the substrate holder is fixed and can be heated up to 700° C while rotating.

7.1.2 Deposition Procedure

The deposition of TiN-Cu coatings was performed by the following steps:

- The substrates were ultrasonically cleaned both in acetone and in ethanol each for 5 minutes and afterwards air dried.
- The substrates were fixed to the sample holder and mounted in the deposition chamber.
- The evacuation of the sputtering system was started. By the time the pressure reaches 2x10⁻³ Pa the heating of the substrates was started.
- After the temperature reached 400° C and the vacuum was down to 2x10⁻³ Pa again the substrates were plasma etched: Therefore, a plasma was ignited in pure argon atmosphere. The etching voltage and the etching frequency were set to -500 V and 250 kHz, respectively. Depending on the substrates, Si or S 600, the etching time was 5 and 15 min, respectively.
- Subsequent to etching the plasma at the magnetrons was started, the deposition parameters were set, the rotation of the sample holder was turned on and with the opening of the shutters the deposition was started. First a thin interlayer of TiN was deposited to enhance the adhesion of the coating.
- Depending on the structure of the coating either all three shutters were open at the same time (forming a nanocomposite) or the Ti shutters or the Cu shutter are opened alternately (resulting in a layered structure). Furthermore, a bias voltage of -50 V was applied to the substrates during the deposition of a nanocomposite. When forming a bi- or multilayer, bias voltages of -20 V for Cu and -80 V for TiN respectively, were applied. The flow rates of the reactive gas (N₂) and the working gas (Ar) were kept constant at 3 and 30 sccm during deposition.
- When the deposition was finished the power supplies, the sample holder rotation and the heating system were turned off. After cooling down to 60° C the pumping system was shut off, the chamber was vented and the substrates were dismantled.

7.1.3 Substrates and Targets

Three types of substrates have been used in this work:

- Single crystal silicon (100) discs of two different sizes:
 - 20 x 7 x 0.2 mm for multilayer structures
 - 20 x 7 x 0.3 mm for nanocomposite layers

The measurements carried out at these samples were: coating thickness, structure analyses, biaxial stress temperature measurement and the thicker ones were used for TEM sample preparation.

- Böhler S600 (DIN 1.3343, AISI M2) high speed steel discs of $\varnothing 30 \times 10 \text{ mm}^3$ in size. These circular blanks were used for tribological testing, evaluation of adherence and nanoindentation.

For the deposition two kinds of targets have been necessary:

- Titanium: dimension $\varnothing 50.6 \times 6 \text{ mm}$
- Copper: dimension $\varnothing 50.6 \times 6 \text{ mm}$

7.1.4 Coating Deposition Parameters

In a previous step, some depositions were done to determine the appropriate deposition parameters. TiN coatings have been produced to evaluate the required N_2 partial pressure to obtain a stoichiometric TiN. Additionally, pure Cu films were deposited to define the adequate temperature for a smooth surface and the deposition rate. Furthermore, TiN as well as Cu were both sputtered simultaneously with varying power on the Cu-magnetron. This leads to a nanocomposite with different Cu fractions.

As a result of these preliminary tests, following parameters were chosen:

- The $p_{\text{N}_2}/(p_{\text{N}_2}+p_{\text{Ar}})$ ratio of 9% at $p_{\text{tot}} = 0.25 \text{ Pa}$ is the optimum parameter for stoichiometric TiN.
- A temperature of 400°C leads to a uniform Cu surface.
- The dependence of the coating chemical composition as function of the magnetron power were determined and represent the base of the power settings chosen (parameters are shown in Figure 7.2).
- To realize a constant film thickness of $3 \mu\text{m}$ with varying Cu contents, the different deposition rates and the necessary deposition times were determined (see Figure 7.3).

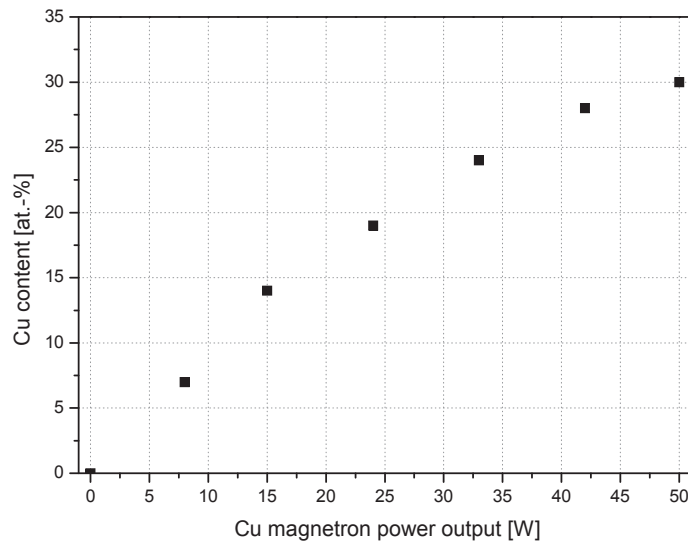


Figure 7.2: Dependence of the chemical composition of the nanocomposite coating as a function of the Cu magnetron power

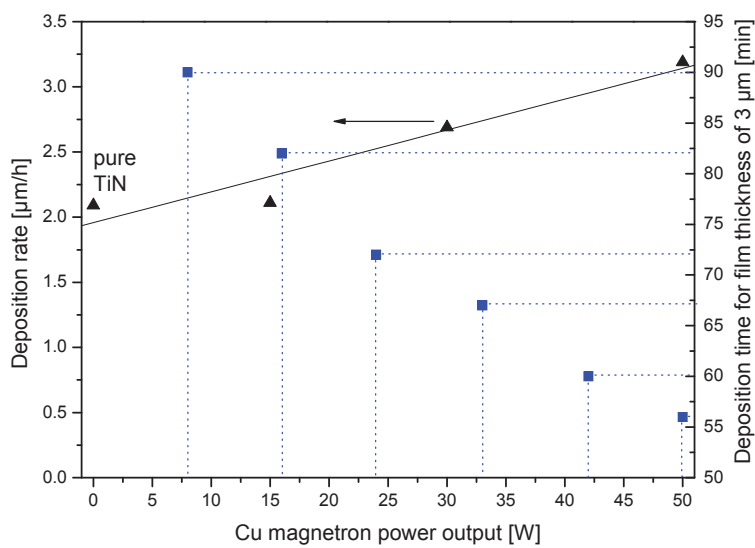


Figure 7.3: Variation of the deposition rate as a function of the Cu magnetron power output and deposition times for different currents by constant film thickness

Parameters for the three different types of coatings used in this thesis:

Bi-Layer (BL): $T = 400^\circ \text{C}$
 $p_{\text{tot}} = 0.25 \text{ Pa}$
 Bias voltage: Cu = -20 V
 TiN = -80 V

TiN magnetron current: 0.7 A

Cu magnetron power output: 150 W

Different sputtering times for pure Cu to obtain different layer thicknesses (50, 100, 200 and 400 nm).

Constant deposition time for the top TiN-coating (500 nm).

Multilayer (ML):

T = 400° C

$p_{\text{tot}} = 0.25$ Pa

Bias voltage: Cu = -20 V

TiN = -80 V

TiN magnetron current: 0.7 A

Cu magnetron power output: 150 W

Different sputtering times for Cu and TiN to obtain varying layer periods ($\Lambda = 100, 200, 400$ and 800 nm)

Nanocomposite (NC): T = 400° C

$p_{\text{tot}} = 0.25$ Pa

Bias voltage = -50 V

TiN magnetron current: 0.7 A

Different Cu magnetron powers and deposition times (see Figure 7.2 and Figure 7.3)

7.2 Coating Characterisation

7.2.1 Coating Adhesion

To evaluate the adhesion of the nanocomposites coatings to high speed steel substrates, a Rockwell indentation test (Rockwell C, DIN 50103 Part 1) was performed. An image of the indent was obtained using a light microscope and then classified according to the adhesion table shown in Figure 7.4. This scheme illustrates six categories, where HF 1 exhibits the best adherence. In this case just a fine crack network encloses the indent. This crack network intensifies until HF 4 where the adherence worsens. In case of HF 5 and HF6 the coating already delaminates, which is a sign of worst adherence. Coatings with HF 5 and HF6 adhesion are not suitable for technical applications [74].

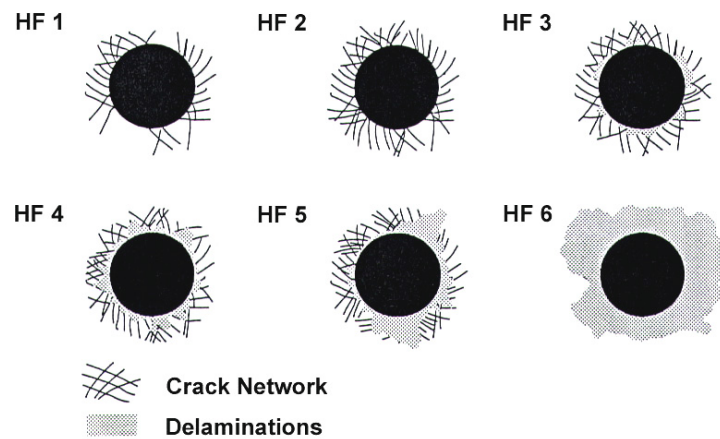


Figure 7.4: Six categories of adhesion by Rockwell indentation [74]

7.2.2 Coating Thickness

Many properties of a thin film, such as residual stress and coating adherence, depend on its thickness. Moreover, the knowledge of the film-thickness t_c is an important parameter for further investigations such as nanoindentation. There are several methods of measuring the thickness of a coating which can be divided into destructive and non-destructive methods. In this work a Calotest[®] tester of CSM was used to perform the so called ball-crater-test, which belongs to the destructive methods [75].

A steel ball of diameter D rotates on the sample surface while a diamond suspension serves as an abrasive. The fundamental function is illustrated in Figure 7.5. As a result, a round wear crater is induced on the sample.

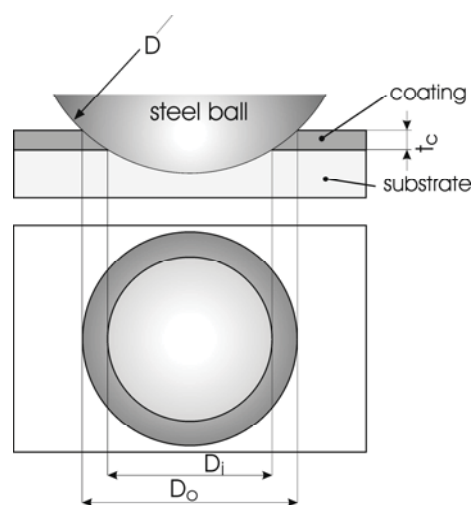


Figure 7.5: Schematic view of the ball-crater-test [28]

If the crater is deep enough, the thickness of the film can be calculated with Equation 7.1 [74]:

$$t_c = \frac{D_0^2 - D_i^2}{8D} \quad \text{Equation 7.1}$$

The outer diameter (D_0), which marks the film surface, and the inner diameter (D_i), which marks the interface between surface and substrate, are determined in a light optical microscope. The section through the film should incline as gentle as possible in order to obtain precise values of the diameters, so that the thickness can be evaluated with small errors.

7.2.3 Scanning Electron Microscopy (SEM)

Structure, chemical composition and wear tracks were investigated with a scanning electron microscope (Zeiss Evo50 SEM). To determine the chemical composition of the coatings, the attached energy-dispersive X-ray analysis equipment (Oxford Instr. INCA EDX) with Co-standard was used.

Images of the surfaces and cross-sections of the coatings and the wear tracks were recorded with secondary electron imaging mode. Secondary electrons (SE) have energies lower than 50 eV and are emitted by the specimen under irradiation of the electron beam. Because of their low energy they emerge from thin surface regions (3-10 nm) and thus, carry high resolution information. In addition, the backscattered electron imaging mode has been used to obtain further images of the wear tracks. Characteristically, these images often allow a phase distinction as contrast changes with varying atomic weight. Backscattered electrons (BSE), which have been scattered by the Bragg Law, have high energies, because they are incident electrons. The probability of backscattering rises with increasing atomic number Z , but elements with lower Z than carbon can not be detected [76].

7.2.4 X – Ray Diffraction Analysis (XRD)

X-ray diffraction is a non-contact and non-destructive material characterisation method used for many purposes, such as analyses of: phases, strain state, grain size and crystallographic structure. This method is based on the X-ray reflection at crystallographic planes. The sample is irradiated by a monochromatic X-ray beam (K_0) with an angle of incidence θ . The lattice planes reflect this impinging ray according to the Bragg Law (Equation 8.2). The diffracted beam is detected at an angle of 2θ with respect to the incident beam.

$$n\lambda = 2d_{hkl} \sin \Theta \quad \text{Equation 7.2}$$

n ...class of diffraction, λ ...wavelength,
 d_{hkl} ...interplanar spacing of lattice planes, with Miller indices
 h, k and l , Θ ...diffraction angle between the incoming beam and
the surface of the sample

This mode is called Θ - 2Θ scan and is illustrated in Figure 7.6. The 2Θ angle positions where reflections occur are characteristic for distinct interplanar lattice spacings d_{hkl} . Thus, unknown phases can be specified by comparing crystal structures with data from Joint Committee on Powder Diffraction Standards (JCPDS). Moreover, peak height and breadth state information about grain size, and peak displacement is linked with residual stresses [77].

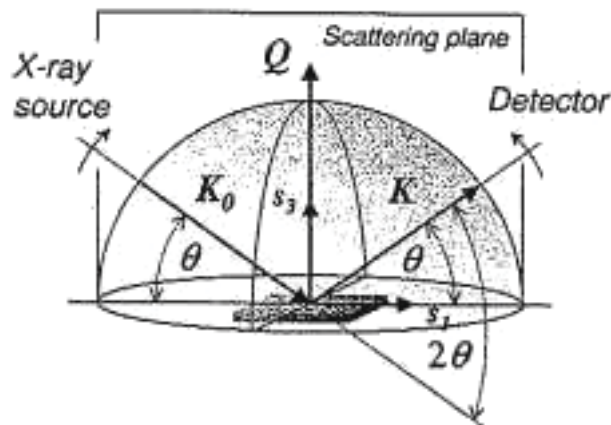


Figure 7.6: Schematic representation of a Θ - 2Θ scan [78]

The XRD-measurements in this work were carried out with a Siemens D500 Diffractometer with Bragg-Brentano geometry using Cu K_{α} radiation ($\lambda = 1.54056$ nm). Further parameters of the XRD structure analysis are: high voltage (40 kV), tube current (30 mA), step time (1.2 s), 2Θ step (0.02°) and 2Θ range (25 - 85°). Since all peaks of interest are in the range of 35 - 65° the axis in the plot has been shortened. Coatings deposited on Si samples were investigated in the as-deposited state and after annealing at 650° C.

7.2.5 Transmission Electron Microscopy (TEM)

During the last century it has become more and more important to know exactly about the internal microstructure and crystal structure of inorganic materials. A fundamental step has been the development of the TEM. The images are formed by an electron beam that passes through the specimen and exhibit microstructural information. The contrast in these images results from different beam scattering or from diffraction produced between elements of the microstructure. Specimens have to be prepared in form of a very thin foil because solid

materials are highly absorptive to electron beams. The transmitted beam is projected onto a fluorescent screen or can be captured electronically. There are two basic modes of TEM operations differing in the ray paths of the electrons: the imaging mode which provides magnification over a range from 100x to 500,000x, or the diffraction mode that provides information about the crystal structure of the sample. [1, 45, 79, 80].

Sample Preparation

Two different nanocomposite samples with 7 and 19 at.% Cu, respectively, were first cut into small (~ 1-2 mm) slices. Afterwards two slices were glued together, coating to coating, to create a sandwich-structure (substrate-coating-adhesive-coating-substrate). The glue (MBond 610 Adhesive Kit, Micro-Measurement-Group, North Carolina) hardened for two hours at about 150° C. This new sample has been stuck with a mounting wax (Electron Microscopy Science) that can be removed again when heated, on the sample holder in that way, that the plains of the sandwich were perpendicular to the abrasive paper. The sample has been manually polished (1, 3, 9 and 15 µm Diamond Abrasive Film, Southbay Technology, California) until a thin foil of 30 µm remained. That followed, the thin foil was glued to a Cu-grid and then ion milled with 3.6 keV Ar ions using a PIPS (Precession Ion Polishing System, Gatan, Model 691). The process has finished when electron transparency occurs.

The measurements were performed by Dr. Limei Cha at the Erich Schmid Institute of Materials Science (Leoben, Austria) using a Philips CM12 operated at 120 kV.

7.2.6 Evaluation of Micro Hardness

The evaluation of the microhardness (H) and the Young's modulus (Y) were carried out with an UMIS nanointender (Ultra Micro Indentation System) from Fischer-Cripps Laboratories. The hardness is determined by the penetration depth. In this case the load during indentation is monitored.

This system uses a special indenter, called Berkovich-indenter, which is a three-sided diamond pyramid with a pointed tip. This pyramid has a nominal angle of 65.3° between the side face and the vertical line and the tip radius is less than 0.3 µm.

The measurements were conducted in the force-controlled mode and during indentation the load-displacement curve was logged. Figure 7.7 illustrates a typical curve. The hardness can be calculated with [81]:

$$H = \frac{P}{A} \cdot \left(\frac{Ai}{A} \right) \quad \text{Equation 7.3}$$

P...indentation force, A...contact area

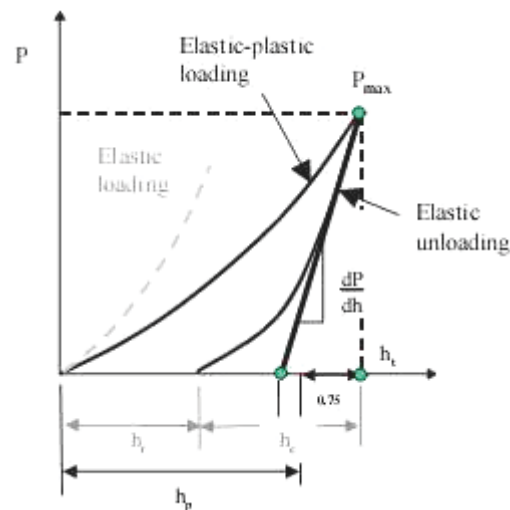


Figure 7.7: Load-displacement curve [81]

The indentation pyramid does not have the ideal shape of a pyramid because of its rounded tip. Therefore in combination with the penetration depth an area function has to be applied to determine the true contact area. Under the assumption of an elastic unloading curve, even if the loading curve shows fractions of plastic deformation, the elastic modulus can be calculated (Equation 7.4) because the slope of the unloading curve correlates with the stiffness (dP/dh) [81].

$$E^* = \frac{dP}{dh} \cdot \frac{\sqrt{\pi}}{2\beta \cdot \sqrt{A}} \cdot \sqrt{\frac{A_i}{A}} \quad \text{Equation 7.4}$$

A_i/A ... stands for the area function

The coatings were tested in the as-deposited state. The device was first calibrated and subsequently the measurements were conducted at maximum loads between 2 and 50 mN with 2 mN steps. When the values are plotted against the indentation depth, a plateau can be seen indicating that the substrate has no influence on the hardness-measurement of the coating.

7.2.7 Biaxial Stress Temperature Measurement (BSTM)

Stress-temperature measurements were conducted to characterise the stress relaxation of the different coatings. In this case the method is called biaxial stress temperature measurement (BSTM) because the stresses are biaxial due to the plate geometry of the samples (see chapter 5.2). The device for this investigation is a self-made unit called "Mutti". To obtain stress relaxation the samples were subjected to a thermal cycle in vacuum ($p \leq 10^{-3}$ mbar). The maximum temperature was 650°C and the temperature has been altered stepwise with a heating and cooling rate of 5 K min^{-1} .

Two parallel laser beams are employed to measure the curvature of the samples by detecting the positions of the reflected beams. A principle setup is shown in Figure 7.8.

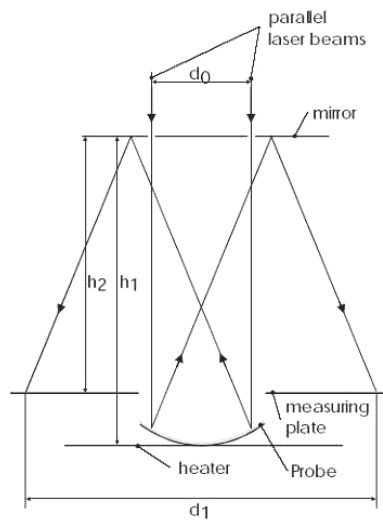


Figure 7.8: Principle of the curvature measurement [28]

The radius of the curvature is determined by d_0 , the distance between the two parallel beams, d_1 , the deflection of the reflected beams, and (h_1+h_2) , the total distance between sample and measuring plane [28]:

$$r = \frac{2 \cdot (h_1 + h_2) \cdot d_0}{d_0 + d_1} \quad \text{Equation 7.5}$$

The samples have been put on the heating plate with the coated side facing the plate. The laser beams which are reflected from the back of the samples are reflected a second time by a mirror. This enlarges the distance between sample and measuring plate, and is necessary to minimise experimental errors.

7.3 Tribological Testing

7.3.1 Friction

A very common testing mode is the so called ball-on disc test. Within this thesis, friction was determined with a ball-on disc tribometer (CSM Instruments THT High-Temperature Tribometer). A schematic illustration of the test device is shown in Figure 7.9. The specimens are fixed by a locking ring on a rotating panel. The counter body, an Al_2O_3 ball, \varnothing 6 mm, is locked in a holder which can be weighted with specific loads ranging form 1 to 20 N. The testing temperature can be set up to 1000°C . During the experiment, the friction coefficient which is calculated from the friction force, is recorded by the software. The test stops automatically when the set sliding distance is reached.

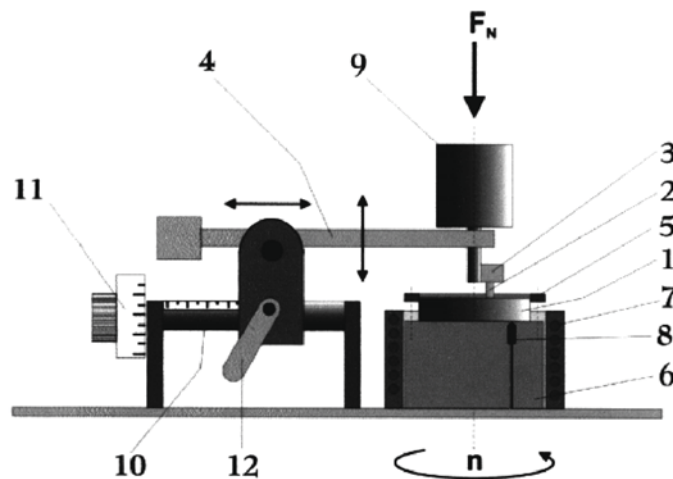


Figure 7.9: Illustration of a high temperature tribometer: 1 sample, 2 ball, 3 ball holder, 4 lever, 5 locking ring, 6 rotation cylinder, 7 resistance heating, 8 thermocouple, 9 cylindrical force, 10 axis for adjustable radius, 11 adjusting screw for radius, 12 lock for the lever arm

Testing parameters:

- Linear speed 0.1 m/s
- Radius 7 mm
- Temperature 25°C , 300°C , 500°C
- Load 5 N (for 25°C), 2 N (for tests performed at 300°C and 500°C)
- Sliding distance 100 m

7.3.2 Nanofocus Analysis

The characterisation of the wear tracks has been difficult, because the surfaces were highly oxidised and rough. The wear tracks were characterise using a NanoFocus[®] μ Surf[®] confocal microscope provided by the MCL (Materials Center Leoben).

The working principle of such a white light confocal microscope is given in Figure 7.10. The light is focused by an objective lens into a focal volume within the sample. Light is reflected on the surface. Light rays which are within the focus pass through the pinhole and are detected by a CCD-Camera. All other light rays, which are not on the same topographic line, are gated out by the pinhole. Subsequently, the measuring head changes its vertical position and another topographical line is detected. Finally all contour lines are assembled to a 2D or 3D picture [82].

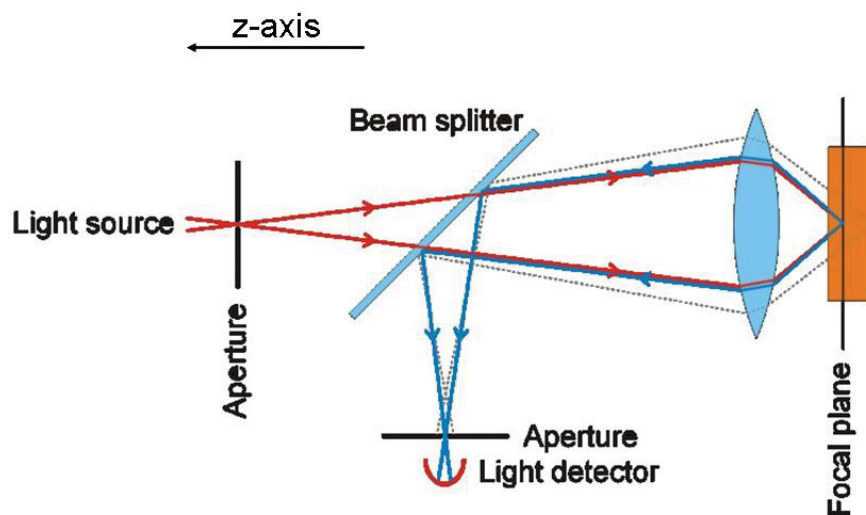


Figure 7.10: Principal of confocal microscopy [83]

8 Results and Discussion

The coatings investigated in this thesis were deposited by reactive magnetron sputtering using Ar as working gas and N as reactive gas. The deposition parameters are listed in chapter 7.1.4. For improved adhesion, a 25 nm thin TiN interlayer was deposited between the substrate and the coating.

8.1 Bi-Layer and Multilayer

The bi-layer coatings investigated in this work consist of a 500 nm thick TiN film and Cu layers of varying thickness (50, 100, 200 and 400 nm). The multilayers consist of alternating Cu and TiN films of same total thickness, where the periodicity (or bi-layer thickness) Λ was varied (100, 200, 400 and 800 nm). The overall thickness of all multilayer coatings was kept constant at 800 nm.

8.1.1 Structure

Figure 8.1 shows XRD-patterns of the bi-layer coatings. The standard peak position of face-centred cubic TiN and Cu are indicated in the figure. The measurements shown in Figure 8.1-**a** were carried out at room temperature (RT), and represent coatings in the as-deposited state. It can be seen that the peaks corresponding to TiN (200) and Cu (111) overlap slightly, but they are definitively separated. The figure clearly shows that the intensity of the (111) as well as the (200) Cu-peaks increase with increasing thickness of the Cu-layer, while the intensity of the TiN-peaks remains constant.

The bi-layer coatings were annealed at 650° C in order to investigate possible structure changes at higher temperatures. Figure 8.1-**b** shows the XRD-scans after annealing. It is remarkable that no significant difference can be found between the patterns before and after annealing: The heights of the different peaks are identical and no peak shift occurs. Concluding, it can be said that no obvious changes in structure occur during annealing.

XRD measurements before and after annealing were also carried out for multilayer films. The results are illustrated in Figure 8.2. Again, the peaks corresponding to TiN (200) and Cu (111) overlap, but they are still clearly separated. The intensity of the TiN (111) peak is very small, and the intensity of the (200) peak increases with increasing bi-layer thickness Λ . The Cu (111) and (200) peaks are both sharp and constant in intensity (Figure 8.2-**a**).

As Figure 8.2-**b** indicates, no apparent structural changes arise from annealing, as the intensities and the peaks positions are almost identical to the as-deposited condition.

Bi-Layer

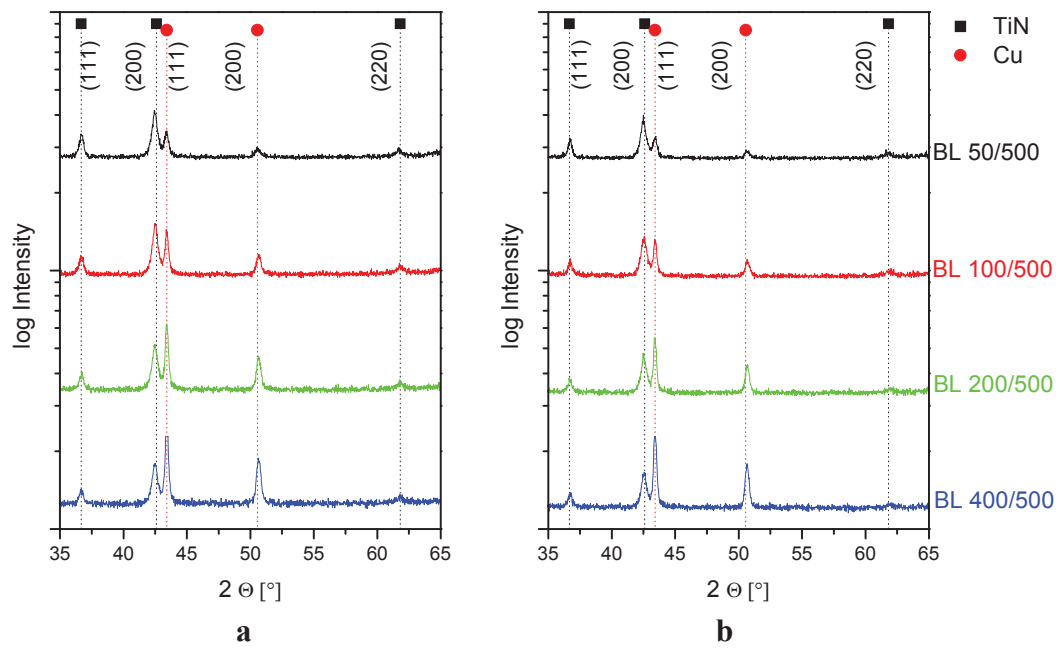


Figure 8.1: XRD patterns for different bi-layer thicknesses on Si (100) substrates; **a** as-deposited state, **b** after annealing at 650°C

Multilayer

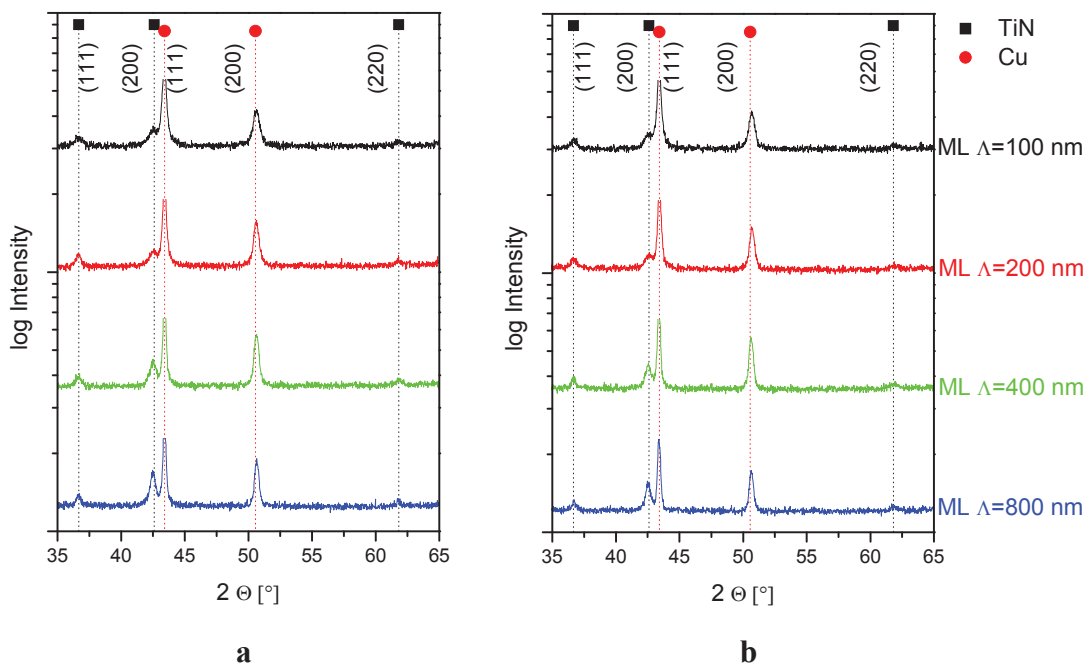


Figure 8.2: XRD patterns for different TiN/Cu multilayer films with different bi-layer thickness Δ on Si (100) substrates, **a** as-deposited state, **b** after annealing at 650°C

Furthermore, the XRD-measurements were used to calculate the domain sizes for the different bi- and multilayers. For all coatings in the as-deposited as well as in the annealed state, the (200)-TiN and the (111)-Cu peaks were fitted with a Pseudo-Voigt function. The broadening of the diffraction-peaks, expressed by the integral breadth (β), was used to calculate the domain sizes of the two phases [77].

As mentioned above, there is no structural difference between the as-deposited state and after annealing in the case of bi-layer coatings. Therefore, the domain size and integral breadth in Figure 8.3 are only depicted for the as-deposited state. As can be seen in Figure 8.3-a, the domain size of Cu increases with increasing Cu-layer thickness, while the domain size of TiN remains constant. The calculated integral breadth for TiN exhibits a similar behaviour; it remains constant whereas that of the Cu-phase decreases for increasing thickness of the Cu-layers (Figure 8.3-b). The integral breadth is the ratio of area under the peak (A) to height of the peak (H) [84]. With increasing thickness of the Cu layer, H increases as well due to the higher amount of Cu in the investigated volume, and thus, β decreases.

In Figure 8.4-a and -b the domain size and the integral breadth of the multilayer coatings are illustrated. Although the XRD-patterns for multilayer in the as-deposited and the annealed state look alike, the domain size of Cu changes during the heat treatment (see Figure 8.4-a). For thin Λ the size in the as-deposited and the annealed state is the same, but the thicker the bi-layer is, the bigger is the domain size after annealing. The domain size of TiN remains relatively constant and furthermore, does not get affected by heat treatment.

The integral breadth of TiN in multilayers decreases with increasing bi-layer thickness in the as-deposited state and do not change significantly after annealing. There seems to be, however, a significant change for the multilayer coating with 100 nm bi-layer thickness. This change is most likely connected with the difficult fitting of the weak signal of the TiN peak. According to Figure 8.2-a, the intensity of the TiN (200) reflection increases with increasing Λ , which is connected with the growth of TiN with increasing film thickness, i.e. smaller grains in the initial stages of growth, and coarsened grains as competitive growth started. This might cause the decrease in β . The integral breadth of Cu also decreases with increasing Λ , and the values are very close to those of the bi-layer coatings.

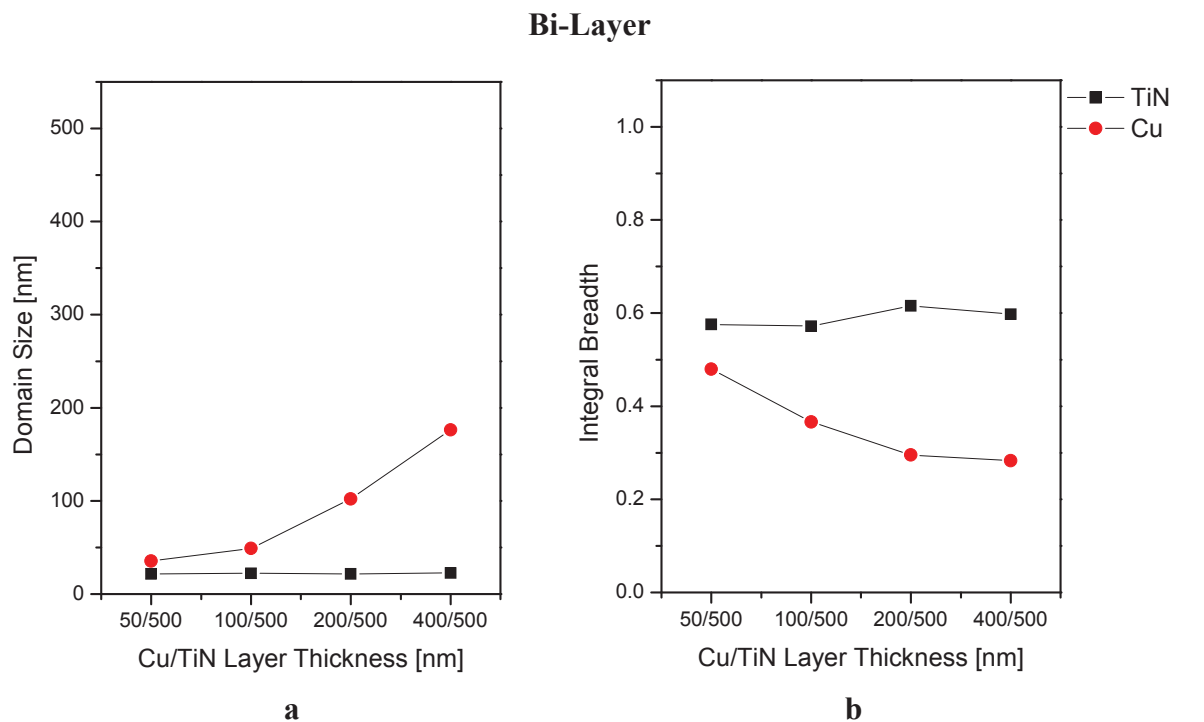


Figure 8.3: **a** Domain size of TiN and Cu for different thicknesses of the Cu layer, **b** integral breadth of TiN and Cu coatings. The data for both figures are calculated from the as-deposited state.

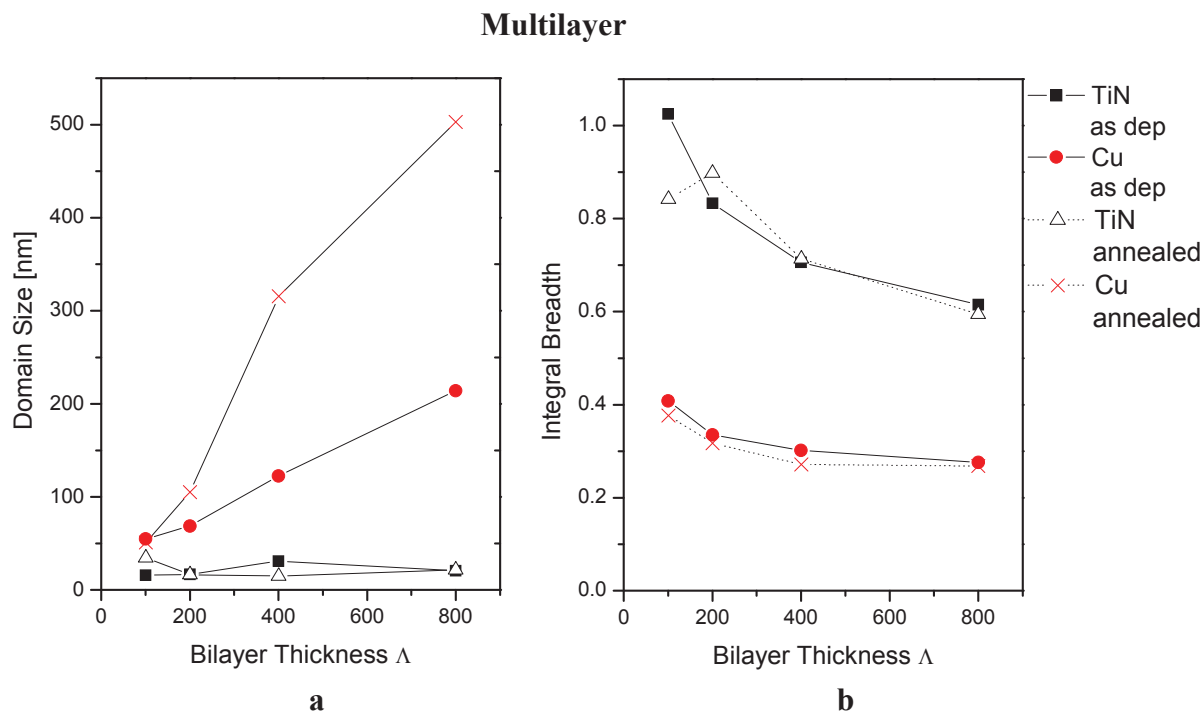


Figure 8.4: **a** Domain size of TiN and Cu for different bi-layer thicknesses Λ , **b** integral breadth of TiN and Cu coatings. Both figures show the as-deposited and the annealed state.

8.1.2 BSTM

Biaxial stress temperature measurements of the bi-layer and multilayer coatings were conducted from room temperature to 650° C during the heating and cooling cycle.

The results of the BSTM cycles for bi-layer films are shown in Figure 8.5. In the as-deposited state (at room temperature) all coatings show intrinsic tensile stresses as a result of the high thermal expansion coefficient of Cu which is constrained between the substrate and the TiN layer. The tensile stresses vary from ~ 20 MPa for the coating with 100 nm Cu layer up to ~ 170 MPa for that with a 200 nm thick Cu layer. During heating, these tensile stresses first relax and then become compressive due to different thermal expansion of the components [85]. Above a temperature of about 300° C all curves reach a plateau and the stress level remains constant up to the maximum annealing temperature. The compressive stresses should normally increase thermo-elastically with increasing temperature. However, two processes might take place above 300° C. First, plastic deformation of the Cu layer occurs which relieves all further stresses. Besides, annihilation of point defects leads to relaxation of intrinsic stresses in the layers as well.

During cooling all bi-layers exhibit linear thermo-elastic behaviour down to 250° C or in the case of BL 50/500 down to 100° C. The resulting tensile stress at RT depends on the thickness of the Cu layer. The thinner the Cu layer is, the higher is the resulting stress. In case of BL 100/500 there is a significant change in the slope at about 250° C, but also the slopes of BL 200/500 and 400/500 change. This change in the slope might be a sign of either crack formation or structural changes. However, no cracks can be found on the surface of the samples, nor can structural transformations be observed according to the XDR-patterns after annealing. Also plastic deformation of the Cu layer due to tensile stresses might be a further explanation for the deviating slope. There is also a tendency of the slopes of the cooling curves to be steeper the thinner the Cu layer is. This might be a consequence of hardening effects in very thin films due to grain refinement (also called size effects) [50, 86].

The BSTM cycles of multilayer coatings are shown in Figure 8.6. In general, they show the same behaviour as the bi-layers since identical mechanisms are governing the stress-temperature behaviour. The coatings show almost same intrinsic tensile stresses of about 150 MPa at room temperature, excepting the multilayer with the thinnest bi-layer thickness ($\Lambda = 100$) that exhibits higher stresses (~ 220 MPa) in the as-deposited state. This anomaly might be also a consequence of size effects. Here again, stresses relieve during heating and become compressive, reaching a plateau at about 300° C. At temperatures above 600° C, the slope of the curve becomes steeper, particularly those of ML Λ 200 nm and Λ 400 nm. Here the stress relaxation due to defect annihilation in TiN phase superposes the plastic deformation of Cu [87]. During cooling down, the multilayer coatings show linear thermo-elastic behaviour, and the slope of the different curves remains constant in a wide temperature range. For the

coatings with $\Lambda = 400$ and 800 nm, the slope slightly decreases for temperatures below 300°C , most likely due to the onset of plastic deformation of the Cu layers under tensile stress.

After cooling down to room temperature, it can clearly be seen that the tensile stresses are higher, the thinner the multilayer coatings are.

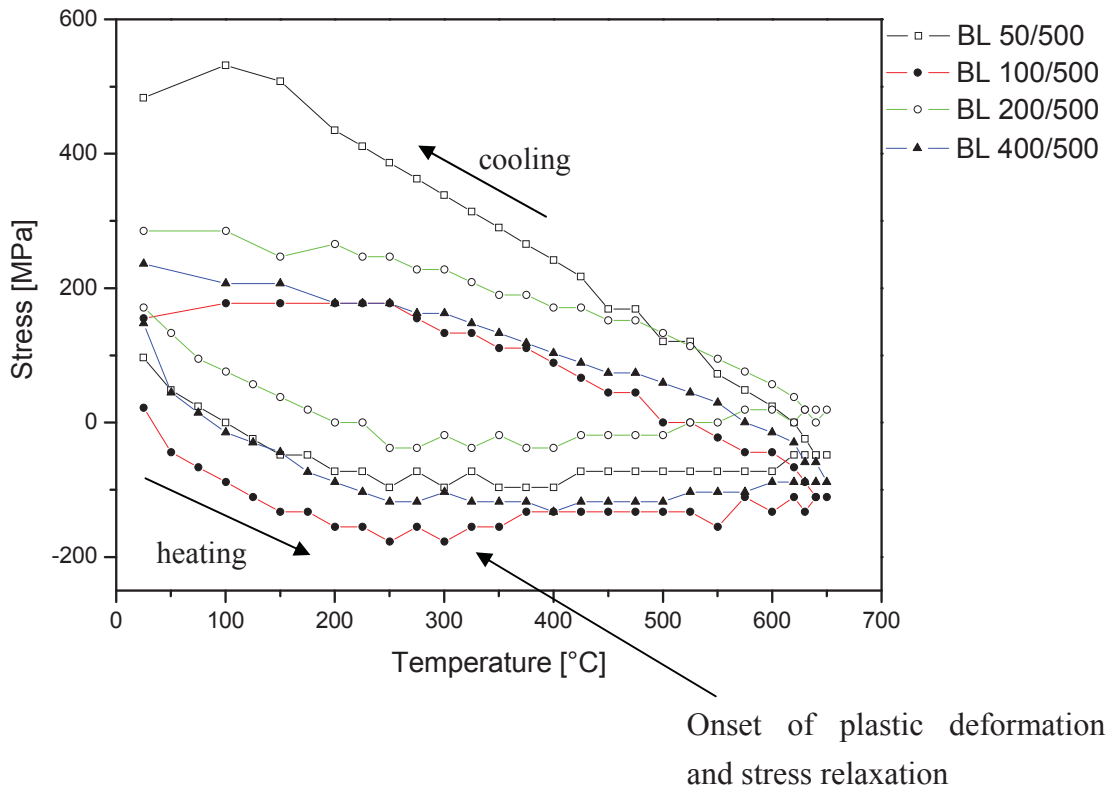


Figure 8.5: BSTM cycles from room temperature up to 650°C of TiN/Cu bi-layer films with different thicknesses of the Cu layer

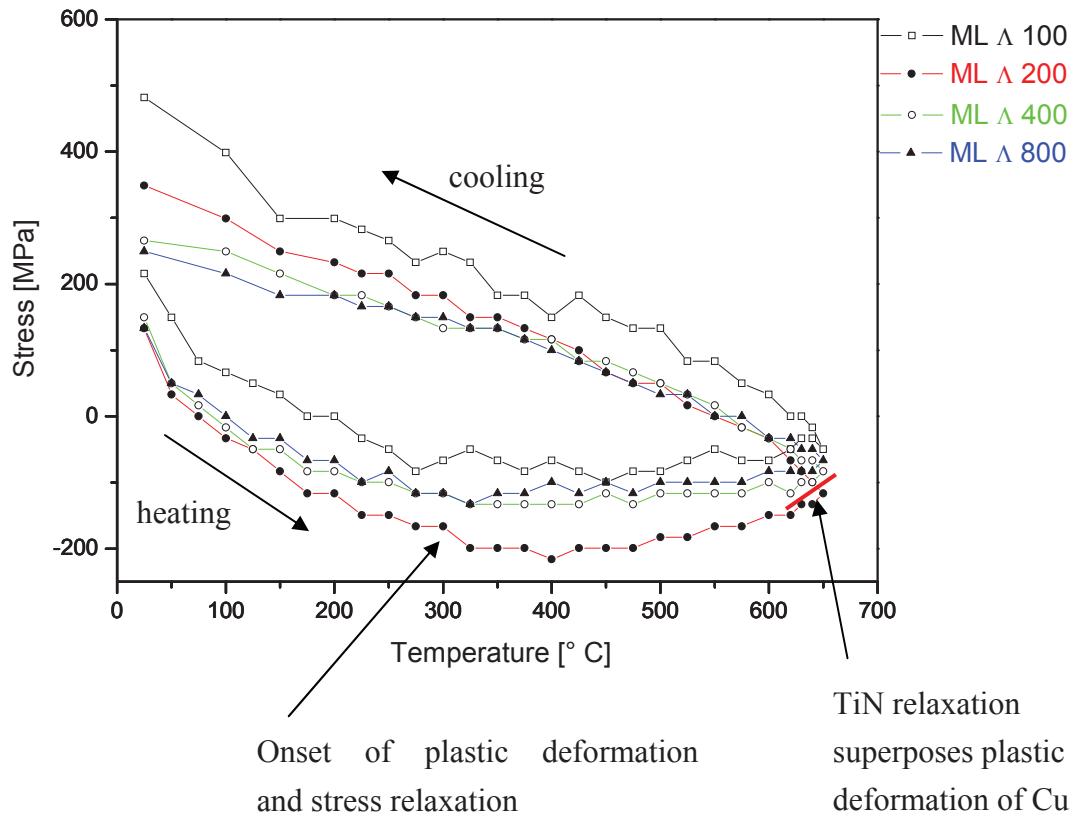


Figure 8.6: BSTM cycles from room temperature up to 650° C of TiN/Cu multilayer films of different bi-layer thicknesses Δ

8.2 Nanocomposite

Nanocomposite coatings consisting of a hard matrix with an embedded second soft phase represent one of the most promising coating architectures for applications where high wear resistance and low friction is needed, but they are also interesting for such applications where stresses due to thermal loading have to be relieved to increase lifetime of a component. In the present chapter, both the stress-temperature and the tribological behaviour of a nanocomposite coating consisting of Cu embedded in a TiN matrix, and the dependency on the Cu content will be elucidated.

8.2.1 Structure

The XRD-patterns of nanocomposite coatings with varying Cu contents in the as-deposited state are shown in Figure 8.7-a. The standard peak positions of TiN and Cu are indicated. The patterns change depending on the Cu fraction, particularly the intensities of peaks, but no peak shift is visible. The intensity of TiN (111) is quite similar for Cu contents between 14 and 30 at.% Cu but it is significantly higher for 7 at.% Cu. The reflections of TiN (200) and Cu (111) overlap for all Cu contents. The presence of two peaks is more evident for Cu fractions above 19 at.% Cu, but the peaks at a 2Θ angle of about 43° are still distinctly asymmetric for 7 and 14 at.% Cu. With increasing Cu content the intensity of Cu (111) increases, whereas the intensity of TiN (200) decreases. Moreover, the smaller the TiN peak the broader it becomes. The presence of two separated peaks for TiN and Cu and the absence of a peak shift for the TiN peaks indicate that two phases without solid solution are formed. The decrease of intensity and the broadening with higher Cu contents suggest a structural refinement of the TiN phase which is also indicated by the domain size in Figure 8.8-a. Besides, the remarkable decrease in the intensity of the TiN (111) peak with increasing Cu content is connected to a change in the preferred orientation of TiN from (111) for 7 at.% Cu to (200) for higher Cu contents.

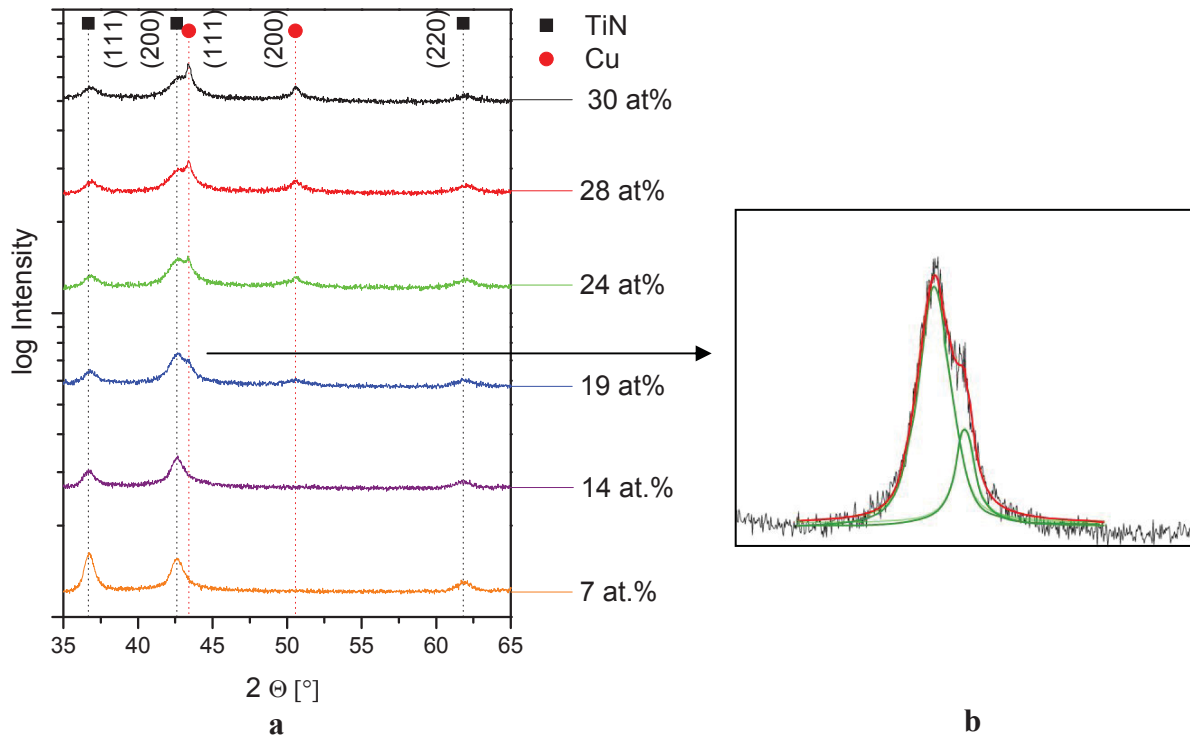


Figure 8.7: **a** XRD-patterns of nanocomposite coatings on Si (100) substrates, **b** schematic representation of a peak fit

Additionally, the domain size $\langle D \rangle$ was calculated from the broadening of the peaks expressed by the integral breadth (β). Two Pseudo-Voigt functions, one for TiN (200) and the other for Cu (111), were fitted to the overlapping peaks as indicated in Figure 8.7-b. The calculated domain sizes and integral breadths are shown in Figure 8.8-a and -b. The domain size of TiN decreases with increasing Cu content and that of Cu increases, while the integral breadth shows the opposite tendency.

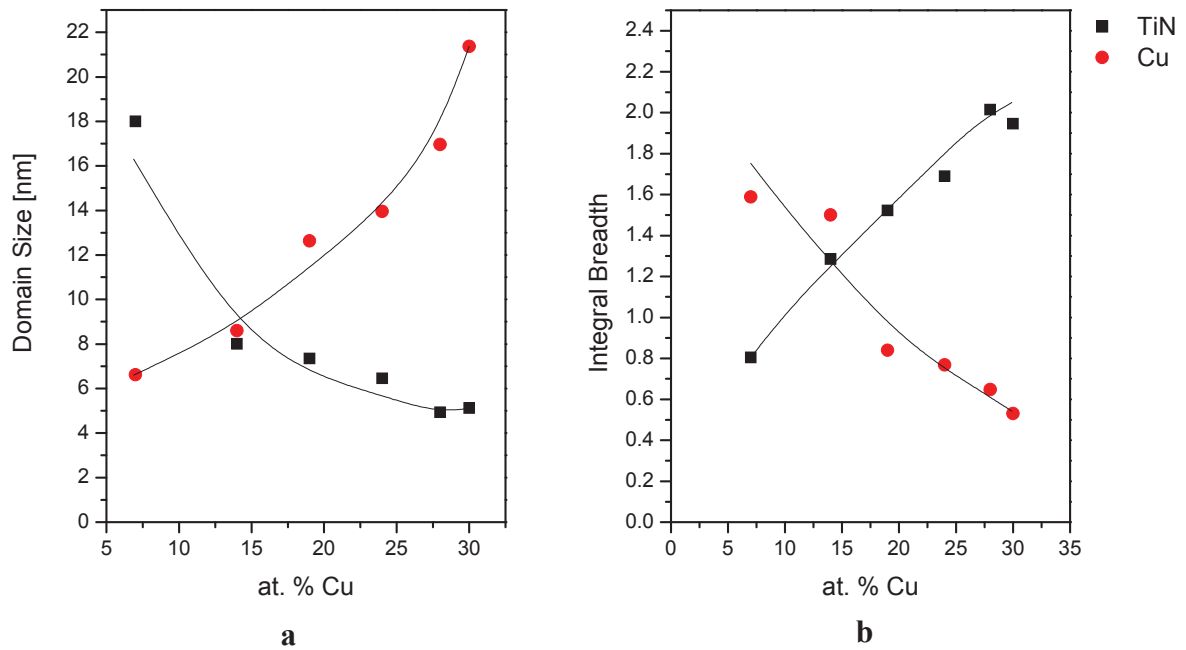


Figure 8.8: **a** Domain size of TiN and Cu for different at.% Cu, **b** integral breadth of TiN and Cu

Nanoindentation of the nanocomposite coatings deposited on high-speed steel discs was conducted. The nanostructured coatings with a Cu content of 7 and 14 at.% show a similar hardness as TiN of about 20-25 GPa [88]. Higher Cu contents clearly reduce hardness of the composite coatings to about 10 GPa (Figure 8.9).

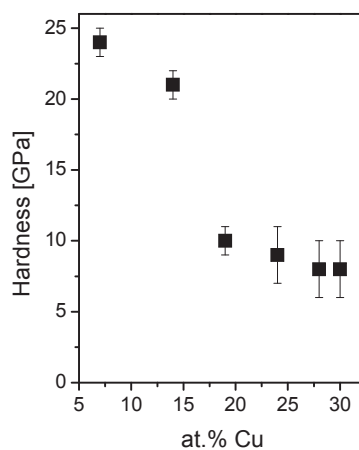


Figure 8.9: Hardness for TiN/Cu nanocomposites with varying Cu content

After annealing at 650° C, XRD measurements of the samples were conducted again. There are significant differences compared to the as-deposited state for higher Cu contents. At a 2θ angle of about 45° a new peak appears which could not be identified (easy to see for 24 and 30 at.% Cu in Figure 8.10). Furthermore, the TiN (200) and the Cu (111) can not be separated even for coatings with high at.% Cu, except for the sample with 28 at.% Cu. However, this coating crumbles during annealing and consequently the XRD measurement was hard to do, and the results are not confiding.

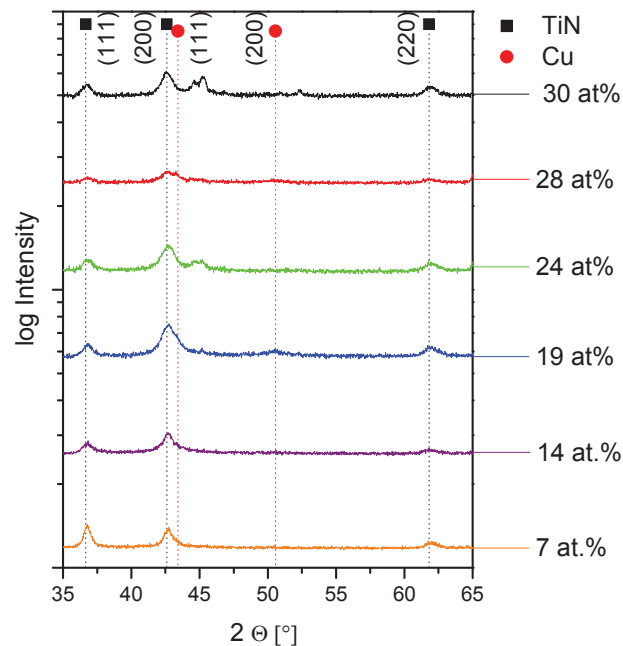
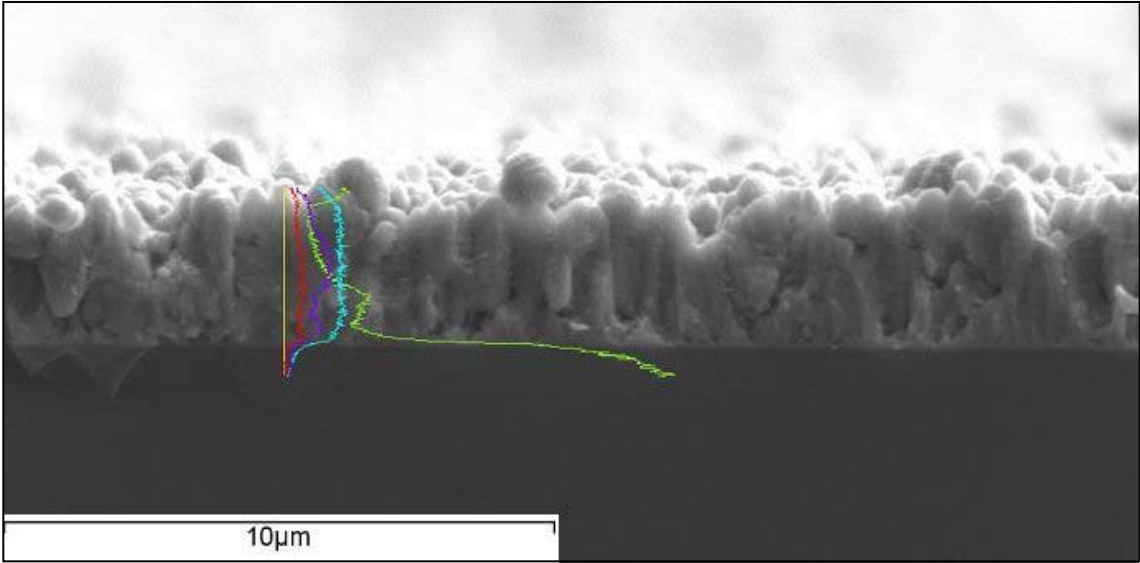


Figure 8.10: XRD-patterns of nanocomposite coatings after annealing at 650° C on Si (100) substrates

For further investigations, the annealed nanocomposite with 30 at.% Cu on Si substrate was broken and analysed by an EDX line scan (Figure 8.11-a). The scan starts at the surface of the coating and shows the distribution of N, Si, Cu and Ti across the film into the substrate. The SEM image exhibits a rough surface and porous columnar structure of the coating.

The content of N and Ti forming TiN in the coating is relatively homogeneous with a slight decrease at the surface (cf. Figure 8.11-b and -c). Cu seems to agglomerate in the middle of the deposited film and close to the coating/substrate interface. At the surface it shows the lowest content (Figure 8.11-d). Unfortunately, Si is found all over the cross section (Figure 8.11-e). This indicates that the applied thin TiN interlayer and the coating itself are not dense and that diffusion occurs during annealing. Based on these findings, the unknown peaks in Figure 8.10 are supposed to result from interacting elements during annealing.



a

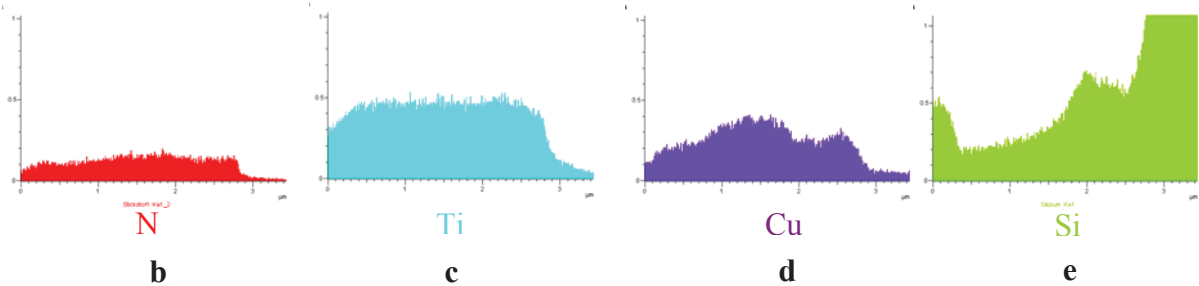


Figure 8.11: **a** EDX line scan of the cross section of TiN/Cu nanocomposites with 30 at.% Cu, distribution through the coating of **b** N, **c** Si, **d** Cu, **e** Ti

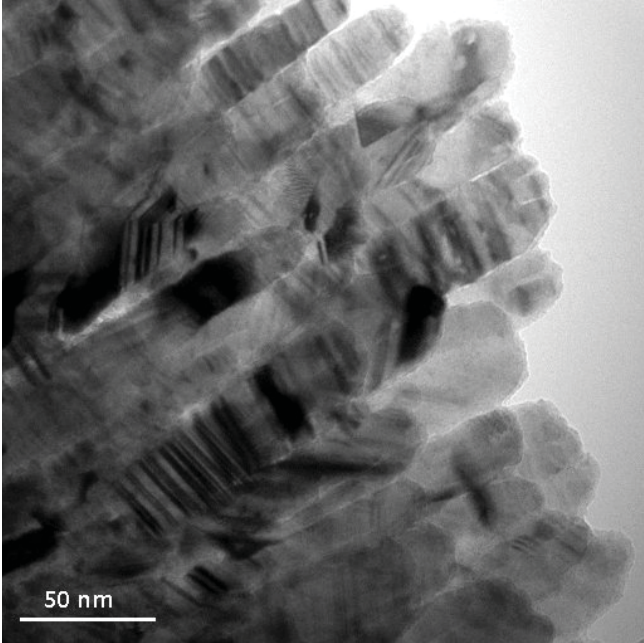


Figure 8.12: TEM bright field image of a cross section of a nanocomposite with 19at.% Cu

The columnar structure has also been approved by TEM investigations (Figure 8.12). Due to the fact that the sample has been glued to a Cu grid and that during the ion milling Cu (of the grid) has been dispersed on the sample, no reliable information about the TiN and Cu distribution in the film can be obtained.

8.2.2 BSTM

The results of BSTM cycles from room temperature up to 650° C for all nanocomposite coatings are shown in Figure 8.13. All coatings except the coating with 14 at.% Cu show tensile stresses in the as-deposited state which are a consequence of the high thermal extension coefficient of Cu. Tensile stresses increase with increasing Cu content. The nanocomposite coating with 14 at.% Cu shows a totally different behaviour, exhibiting high compressive stresses of about -750 MPa in the as-deposited state. Possibly, this might be related to a fully percolated nanocomposite structure with small TiN nanocrystals (~ 8 nm), see Figure 8.8-a, surrounded by a Cu grain boundary phase as described by Patscheider et al. [57]. During deposition, stresses are relieved by plastic deformation of Cu and the more Cu the coating contains, the less compressive stresses exist in the as-deposited state. So, for high Cu contents (19-30 at.%) the observed stresses in the as-deposited state are tensile.

During heating tensile stresses decrease and become compressive while compressive stresses increase because of the higher thermal expansion coefficients of the coating compared to the substrate. At certain temperatures, which depend on the Cu content, the slope of the BSTM curves changes because of plastic deformation and stress relaxation of the Cu phase. All curves except that of the nanocomposite coating with 14 at.% Cu show a plateau at which the stress level remains constant. For coatings with Cu contents of 19 at.% and higher, this plateau is at low compressive stresses compared to the coatings with 7 and 14 at.% Cu. Furthermore, the stress value of the plateau decreases with increasing Cu content.

For the nanocomposite coating with 14 at.% Cu the slope of the BSTM curve changes at ~400° C from positive to negative, which means that with increasing temperature stresses become less compressive.

The plateau is related to the onset of plastic deformation and relaxation processes. As shown in Figure 8.13, the onset temperature decreases from about 410° C for the nanocomposite coating with 7at.% Cu over ~400° C for the nanocomposite coating with 14at.% Cu, to about ~330° C for nanocomposite coatings with Cu contents of 19 at.% and higher. Therefore, the amount of Cu is the determining factor for the onset of stress relaxation and plastic deformation.

The relaxation of stresses in TiN starts at ~600° C, and is most pronounced for the nanocomposite coating with 14 at.% Cu causing a further change in the slope of the BSTM curve. In this case stresses relieve due to defect annihilation in the TiN phase [87].

During cooling the sample with 30 at.% Cu cracks, and therefore, only stress values down to 450° C are shown. The other curves show linear thermo-elastic behaviour down to at least 150° C. The rapid decay in the curves for coatings with 19 at.% Cu and higher at temperatures below 150° C is caused by the formation of micro-cracks and probably plastic deformation due to high tensile stresses. In case of the nanocomposite coating with 28 at.% Cu, delamination of the coating occurred and therefore there are no stresses at room temperature. Only the nanocomposite coatings with 7 and 14 at.% Cu exhibit linear thermo-elastic behaviour down to room temperature.

During cooling, the slope of the curves depends on the Cu content, and the curves are steeper, the lower the Cu content is.

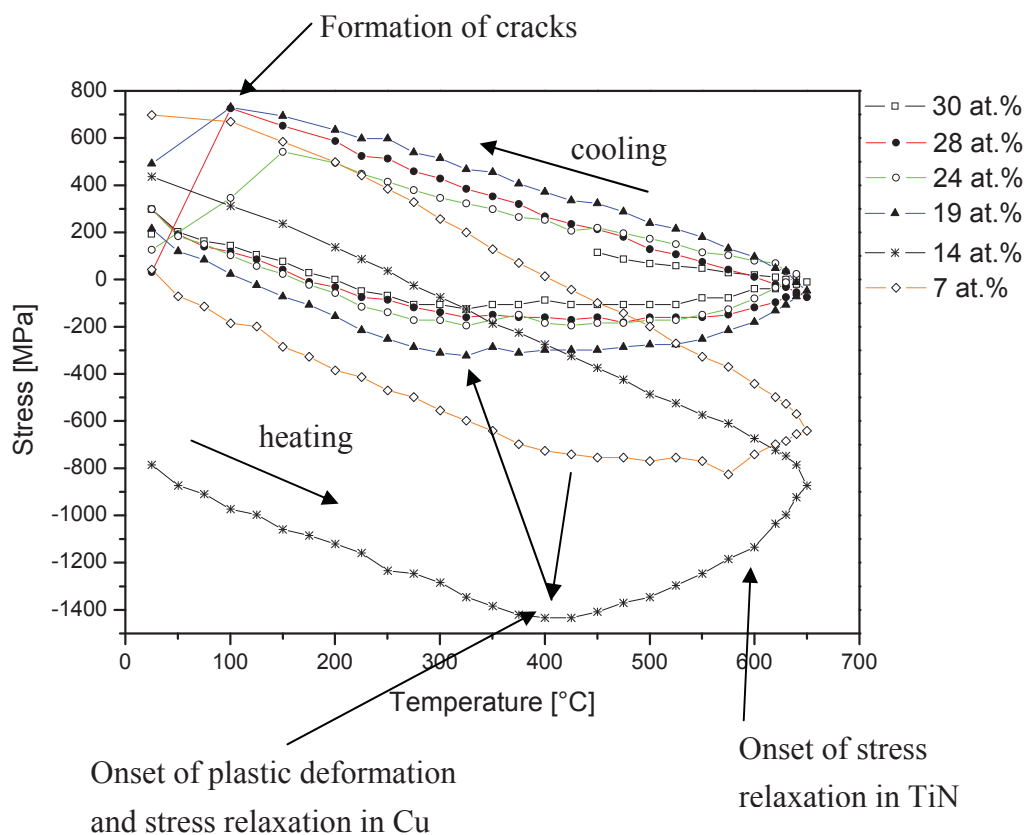


Figure 8.13: BSTM cycles from room temperature up to 650° C of nanocomposite film with different Cu content

8.2.3 Tribological Behaviour

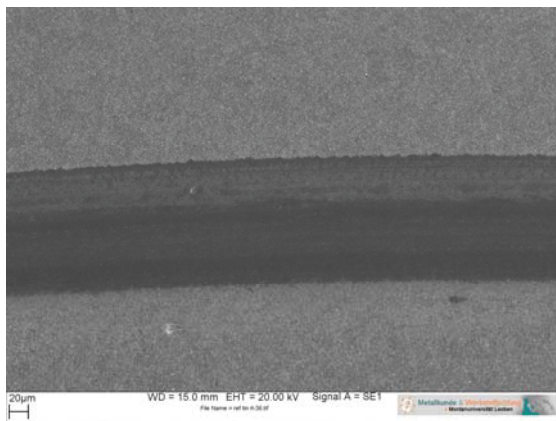
Tribological behaviour has been determined for nanocomposites only, because multilayer coatings shear easily at the interfaces of TiN and Cu and because of the small overall thickness of multilayer coatings. Tribological investigations have been carried out to evaluate the influence of different Cu contents on wear and friction behaviour of the nanocomposite

coatings. The measurements were conducted at three different temperatures (RT, 300° and 500° C) for one sample of each nanocomposite coating. For comparison, a TiN sample grown at $T = 400^\circ \text{C}$, $p_{\text{tot}} = 0.25 \text{ Pa}$, bias voltage = -50 V and TiN magnetron current = 0.7 A is included.

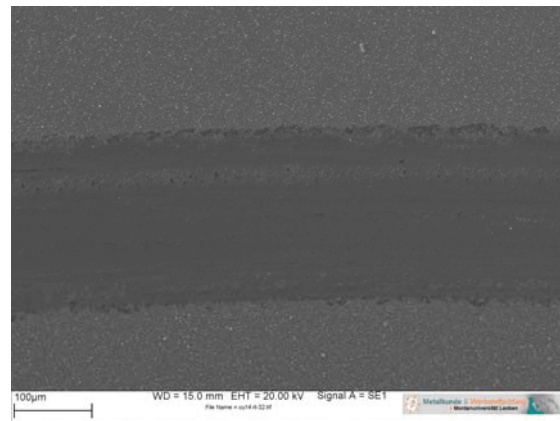
Nanocomposite coatings with similar Cu content show similar behaviour; therefore, three different nanocomposite coatings have been chosen (14, 19 and 30 at.% Cu) which better represent the tendencies in the tribological behaviour, and will be compared to TiN.

8.2.3.1 Room temperature

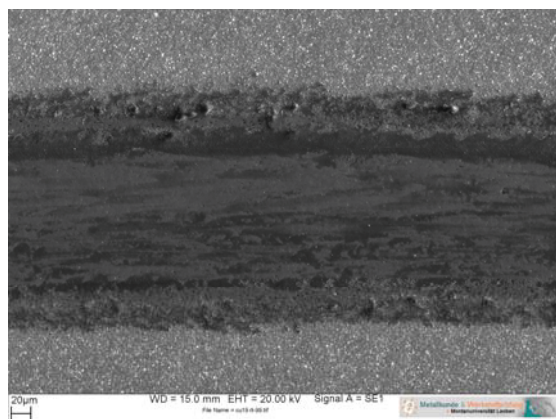
The secondary electron (SE) micrographs of the wear tracks show broadening with increasing Cu content (cf. Figure 8.14). Wear of the coatings at room temperature is mainly caused by abrasion through micro-ploughing and micro-cutting as evidenced by the grooves in the wear tracks (best seen in Figure 8.14-**a** and -**b**). Additionally, the higher the Cu content is the higher is the amount of transferred material in the wear track (see Figure 8.14-**c** and -**d**).



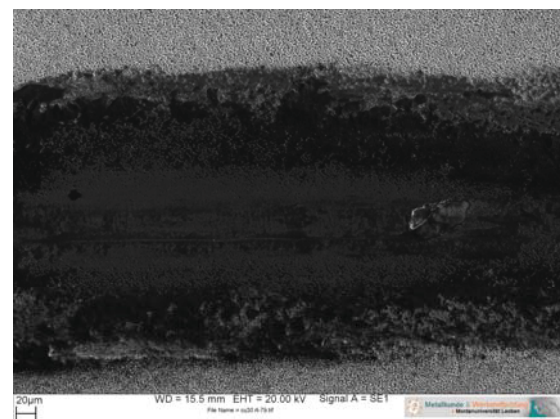
a: TiN



b: 14 at.% Cu



c: 19 at.% Cu

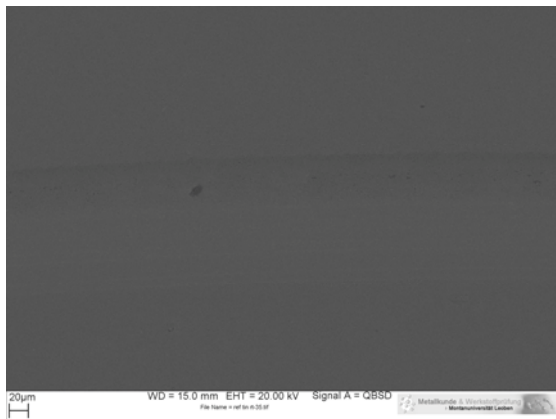
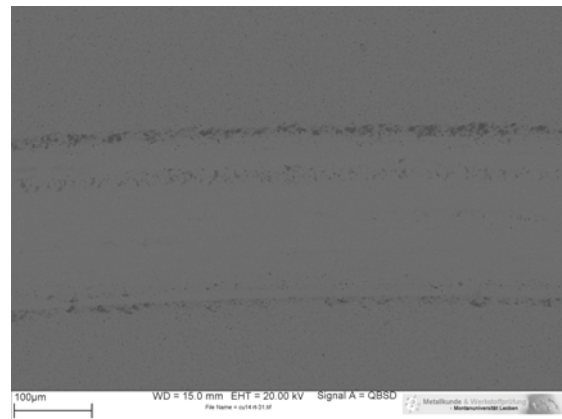
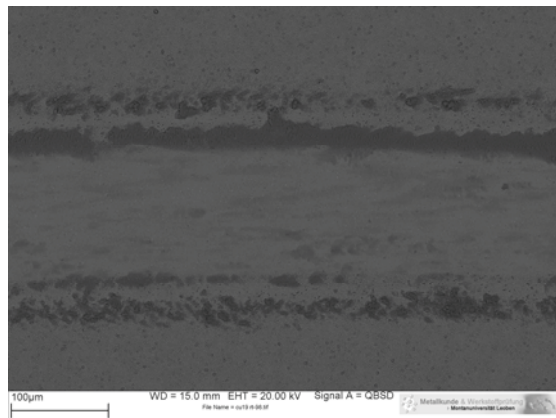
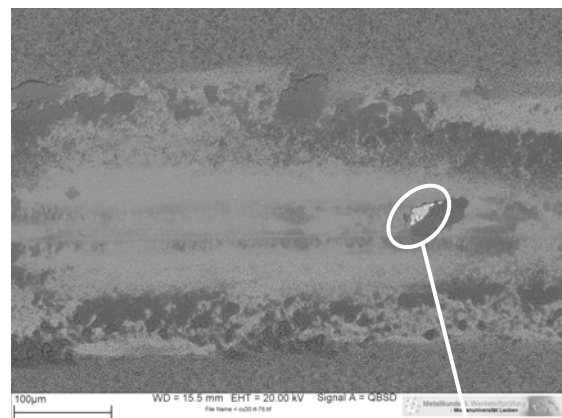


d: 30 at.% Cu

Figure 8.14: SE images of wear tracks produced at room temperature

a TiN, **b** 14 at.% Cu, **c** 19 at.% Cu, **d** 30 at.% Cu

Additional information, e.g. chemical changes during the test like oxidation, can be obtained from back scattered (BS) electron images of the wear tracks. In case of the TiN sample, the wear track is just slightly indicated by darker areas (Figure 8.15-a). In case of the nanocomposite coating with 14 at.% Cu, darker areas appear, especially at both sides of the wear track (Figure 8.15-b). These dark areas represent oxidised transferred material. In Figure 8.15-c and -d these areas considerably increase, and suggest increased oxidation during the test. The brighter areas in the micrographs might indicate the presence of plastically deformed Cu, especially in Figure 8.15-d.

**a: TiN****b: 14 at.% Cu****c: 19 at.% Cu****d: 30 at.% Cu**

Delaminated
area

Figure 8.15: BS images of wear tracks at RT: **a** TiN, **b** 14 at.% Cu, **c** 19 at.% Cu, **d** 30 at.% Cu

The coatings with a Cu content up to 14 at.% have a similar wear behaviour as TiN. For Cu contents above 19 at.%, the wear behaviour changes due to altered mechanical properties, particularly the drop in hardness (cf. Figure 8.9). The heat that has been input by friction leads to oxidation of Cu even at room temperature, and consequently, to higher wear. Furthermore, in Figure 8.15-d the coating is partially delaminated so that the substrate material is visible.

The profiles of the wear tracks confirm the observations of the SEM micrographs. TiN exhibits a small agglomeration of material in the wear track that should have a metallic character, as it could not be identified as oxide in the BS micrographs (Figure 8.16-a). The wear tracks of the nanocomposite coatings tend to be deeper and broader with increasing Cu content (cf. Figure 8.16-b -d). Furthermore, surface roughness increases also with increasing Cu content.

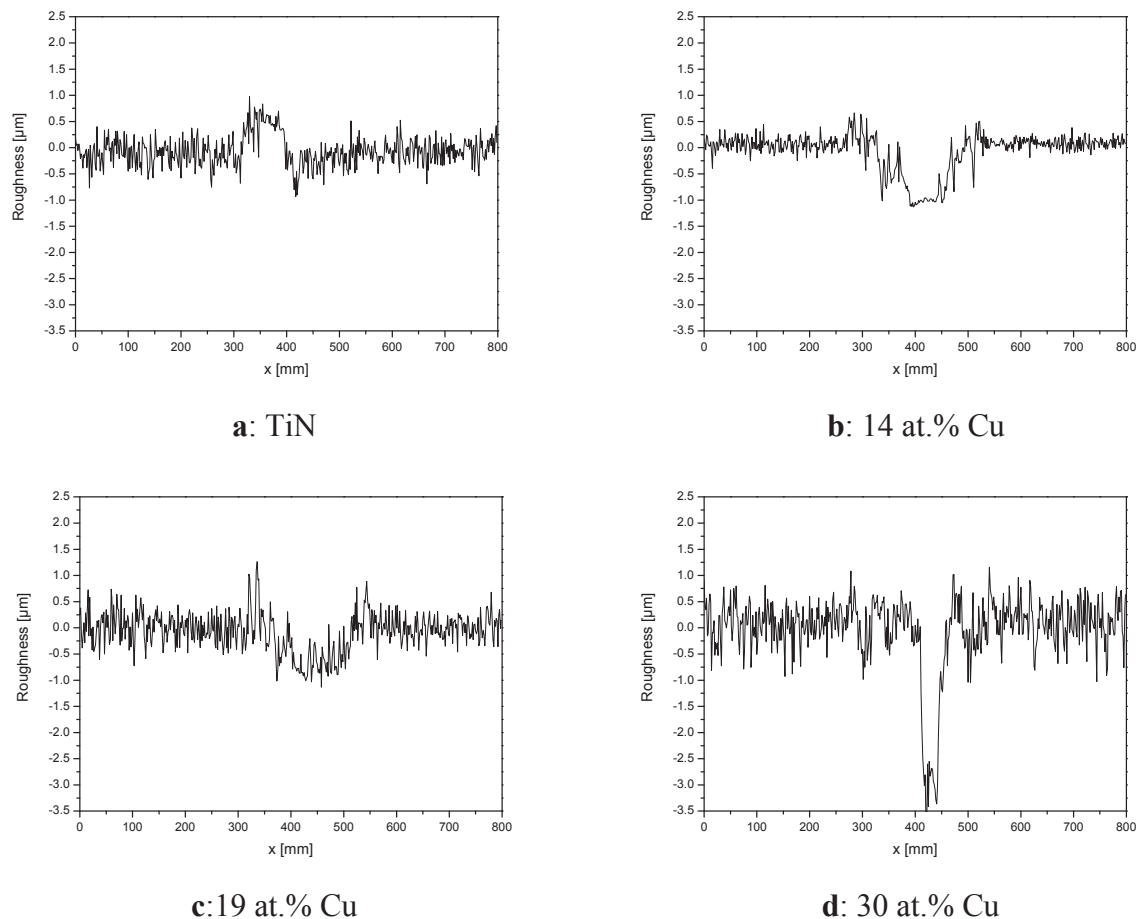


Figure 8.16: 2 D profiles of the wear tracks at RT of: **a** TiN, **b** 14 at.% Cu, **c** 19 at.% Cu, **d** 30at.% Cu

Finally, the evolution of the coefficient of friction over the sliding distance should also be mentioned. After a run-in period, the coefficient of friction remains approximately constant until the end of the test. The steady-state friction coefficient for TiN is ~ 0.7 but for the coating with 14 at.% Cu it increases to values of ~ 0.9 (cf. Figure 8.17-a and -b). This might be connected with interactions of wear debris with the hard coating. With increasing Cu content the coefficient of friction slightly decreases ($0.9 - 0.75$) but it is always higher than that of TiN (see Figure 8.17-c and -d). Furthermore, the scattering of the friction curves increases with increasing Cu content of the coating. This should also be connected to the increasing production of wear debris.

The friction and wear behaviour are influenced by the oxidation of the coating. Removed material quickly oxidises. These oxides are back-transferred to the wear track and protect the coating during the experiment, as described by Stott et al. [89]. This mechanism reduces the wear of the coatings with Cu contents of 19 at.% and above. In case of the nanocomposite coating with 30 at.% Cu, the coating fails as a result of its inferior mechanical properties, and the protection of the coating by oxide scales is not effective.

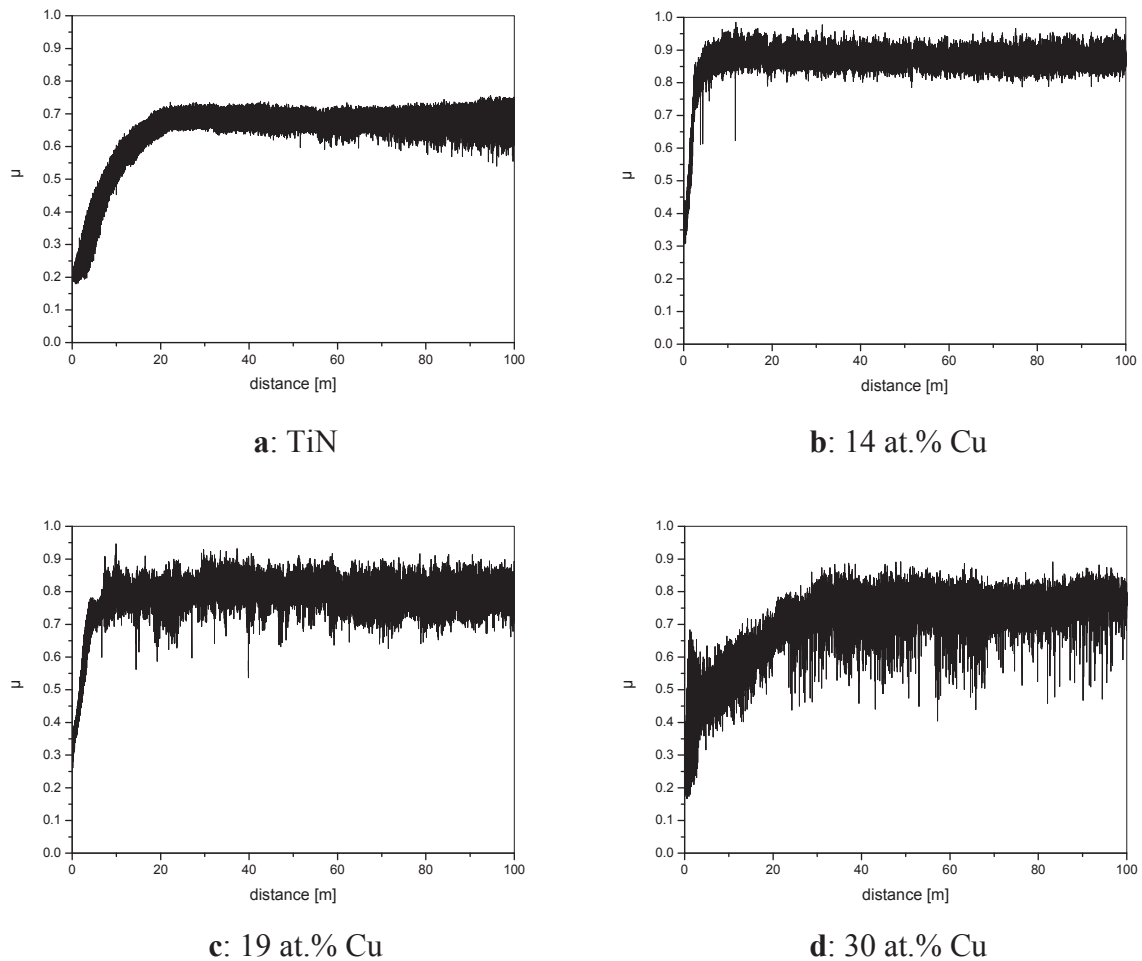


Figure 8.17: Coefficient of friction determined RT as a function of sliding distance

a TiN, **b** 14 at.% Cu, **c** 19 at.% Cu, **d** 30at.% Cu

8.2.3.2 Tribological behavior at 300° C and 500° C

Oxidation of metallic surfaces is the most significant feature at elevated temperatures. The higher the temperatures are, the stronger the oxidation, and wear strongly depends on it. The oxidation resistance of the coatings seems to decrease with increasing Cu content. This result in deeper and broader wear tracks at 300° C (cf. Figure 8.18-a-d), where the wear mechanism seems to be mild abrasion. The coefficient of friction does not vary significantly for the different coatings, and is about 0.6, but scattering is very pronounced (cf. Figure 8.19-a-d). Both the decrease in the coefficient of friction and the higher scattering compared to room temperature are connected to oxide formation and the subsequent debris formation.

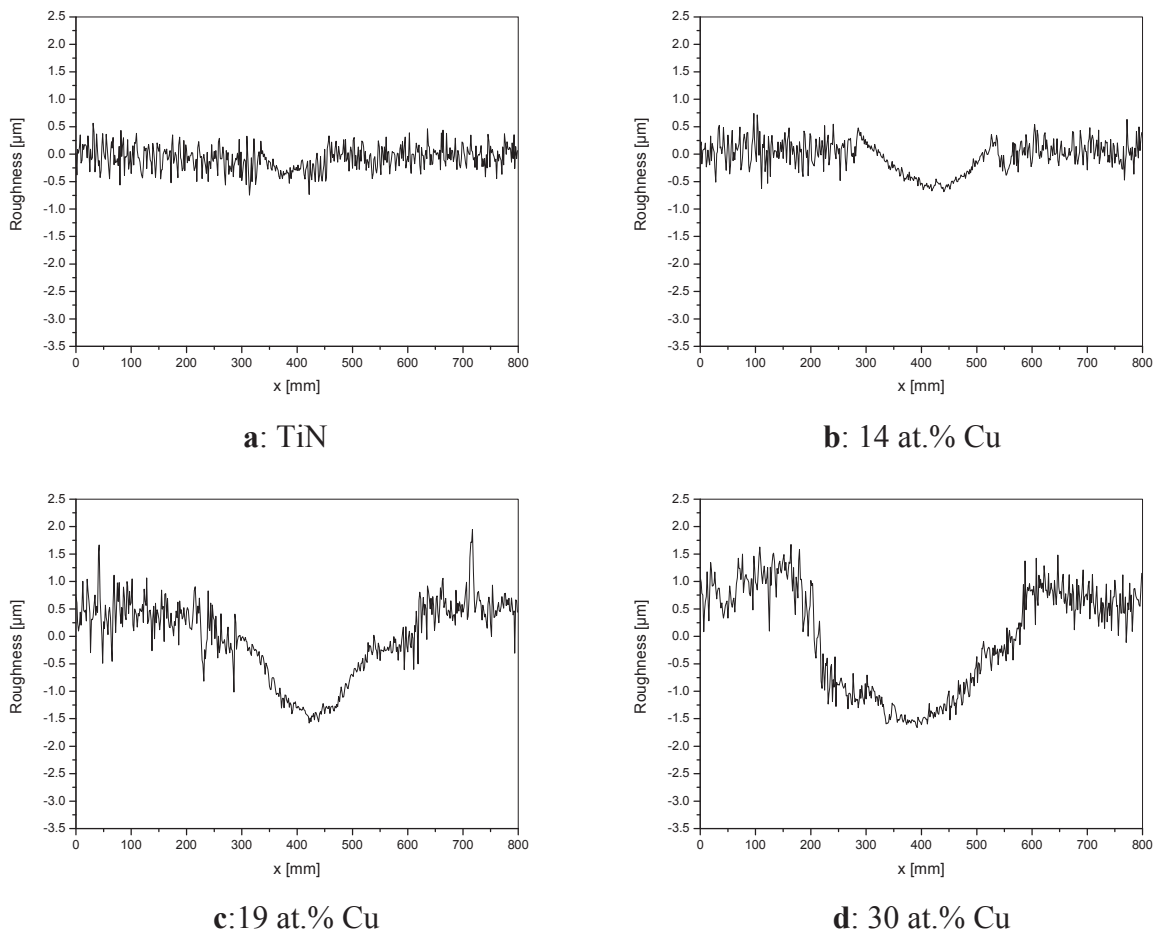


Figure 8.18: 2 D surface profiles of the wear tracks after testing at 300° C:

a TiN, b 14 at.% Cu, c 19 at.% Cu, d 30at.% Cu

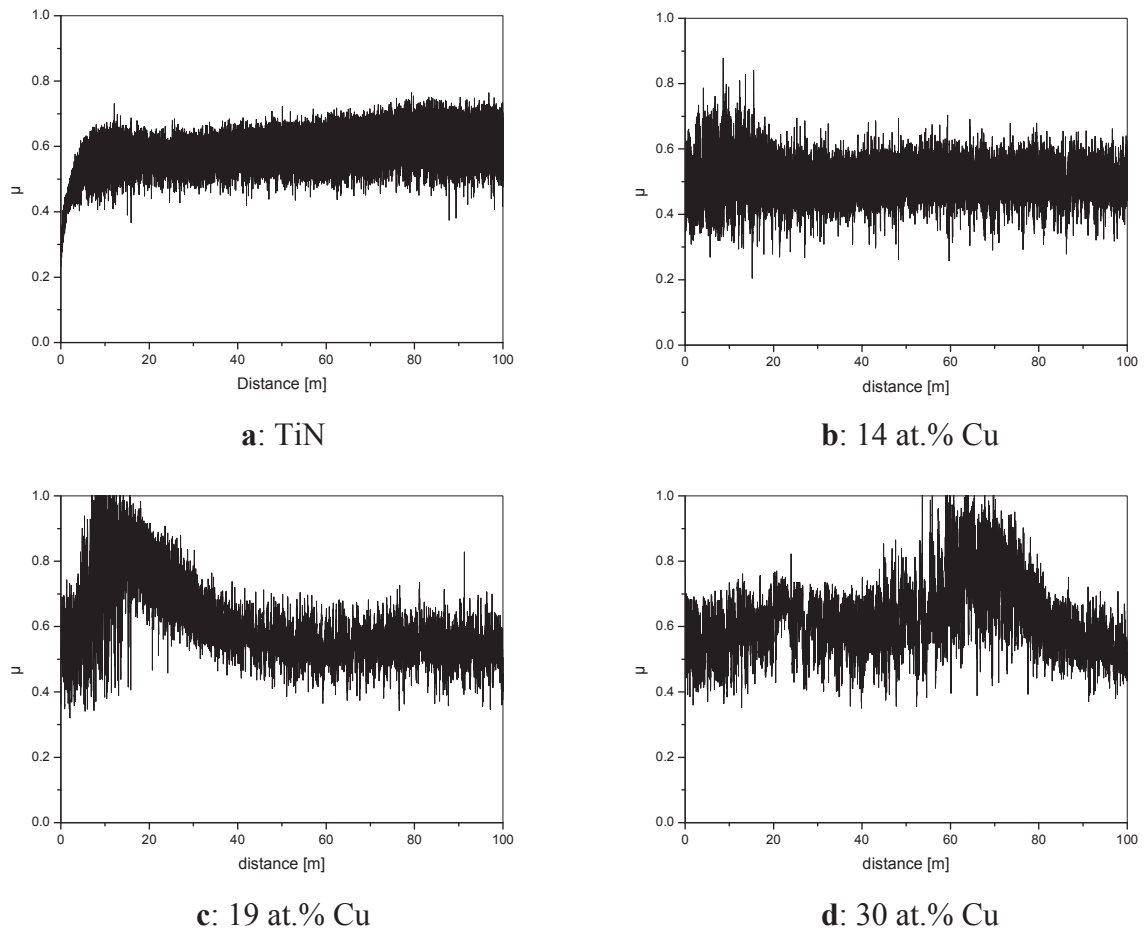


Figure 8.19: Coefficient of friction determined at 300° C as a function of sliding distance

a TiN, **b** 14 at.% Cu, **c** 19 at.% Cu, **d** 30at.% Cu

At 500° C the situation is very similar to the results of the tests at 300° C. Oxidation influences the wear behaviour of the coating resulting in wear track profiles similar to Figure 8.18. The wear track becomes broader and deeper, and the amount of oxides in the wear track increases with increasing Cu content. The BS micrograph of TiN does not show any differences in chemical composition between wear track and oxidised surface outside the wear track (Figure 8.20-a). However, oxides in the wear track are present in case of the nanocomposites coatings (Figure 8.20-b-d).

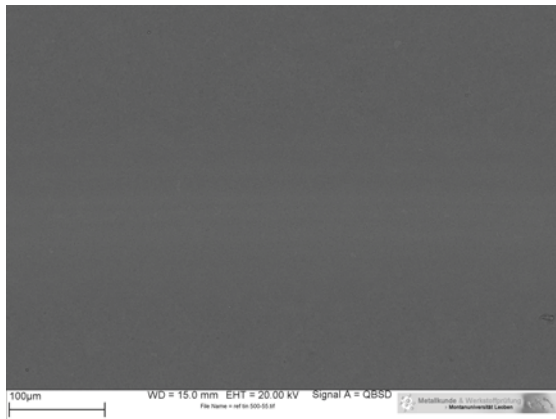
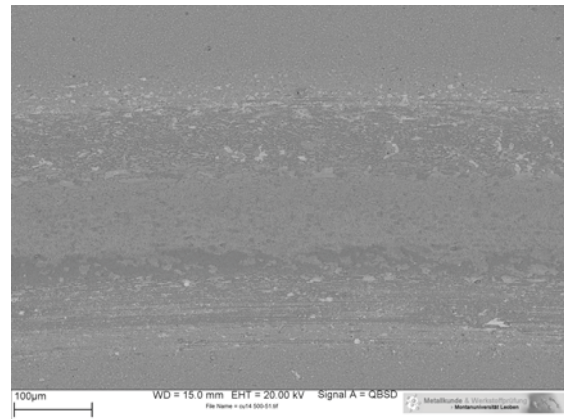
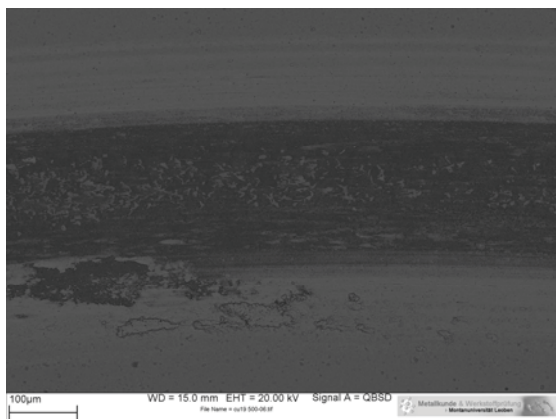
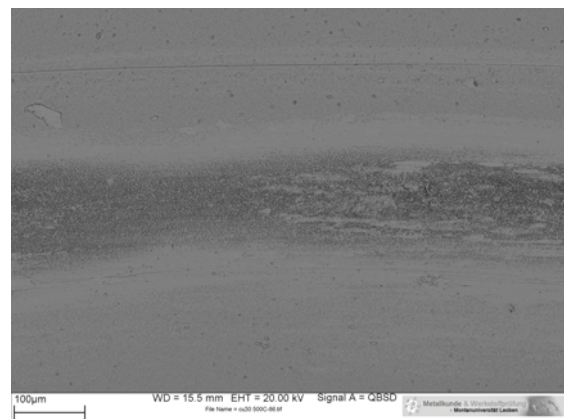
**a: TiN****b: 14 at.% Cu****c: 19 at.% Cu****d: 30 at.% Cu**

Figure 8.20: BS images of wear tracks of the coatings investigated at 500° C
a TiN, **b** 14 at.% Cu, **c** 19 at.% Cu, **d** 30at.% Cu

The coefficient of friction slightly decreases from 0.5 to 0.35 with increasing Cu content (Figure 8.21). The loss of mechanical properties (less hardness leads to less friction) and oxide formation might be the reason for this behaviour [90].

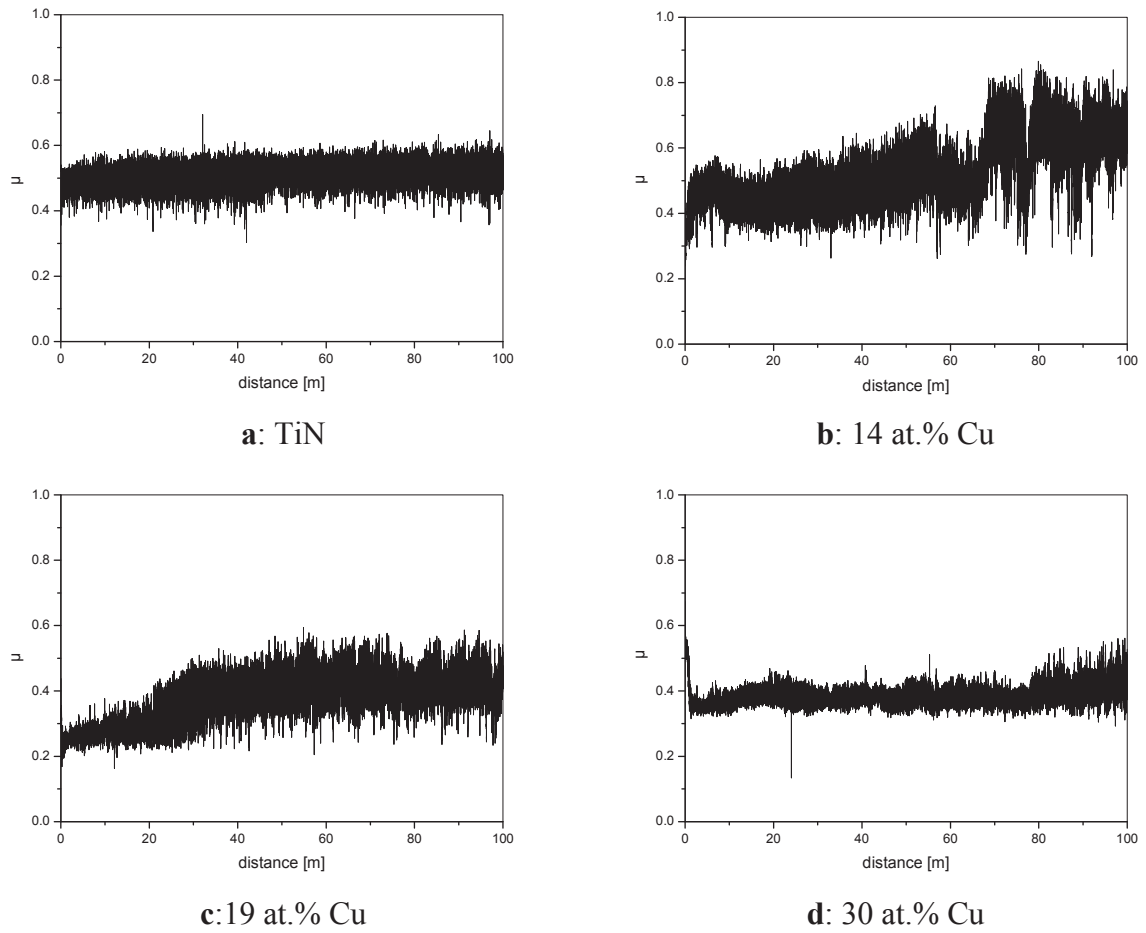


Figure 8.21: Coefficient of friction determined at 500° C as a function of sliding distance

a TiN, **b** 14 at.% Cu, **c** 19 at.% Cu, **d** 30at.% Cu

9 Summary and Conclusion

Microstructural and compositional changes of hard coatings during use are of major interest to extend lifetime and prevent early failure of tools or components. The performance of advanced hard coatings utilised in thermally loaded applications strongly depends on structure and stress behaviour. Stress-temperature behaviour of single-phase coatings like TiN or CrN has already been investigated in detail in the literature. In this thesis, a more complex system represented by TiN/Cu relying on the basic understanding of the processes in TiN has been investigated. The TiN/Cu system was chosen for evident distinction of the influences of the individual phases TiN and Cu on the system. For more detailed information, two different coating structures (multilayered and nanocomposite) deposited by unbalanced magnetron sputtering were examined.

Multilayered coatings, divided into bi-layers with varying thicknesses of the Cu-layer and multilayered coatings with different periodicities Λ , show apparently no changes in structure between the as-deposited and the vacuum annealed state (650° C) determined by XRD-measurements. For further information domain sizes were calculated from XRD patterns. The domain size of Cu in bi-layers increases with increasing Cu content in the coating whereas it stays constant for TiN. No change in domain sizes occurs during annealing. Multilayers exhibit a slightly different behaviour. The domain size of Cu increases, the thicker the bi-layer is and increases even more after a heat treatment. The domain size of TiN remains relatively constant and does not get affected by annealing. Contrary, the structure of nanocomposite coatings with varying Cu contents does change during annealing. XRD-patterns for Cu contents > 19 at.% exhibit a new peak at about 45° which could be attributed by an EDX line scan to reaction products with Si from the substrate, which was found all over the film cross section. This indicates that the coating is not dense, which was also approved by TEM investigations, thus enabling diffusion during annealing. For nanocomposite coatings the domain size of Cu has only been calculated for the as-deposited state and is increasing with increasing Cu content while the domain size of TiN decreases.

For all kinds of coatings, biaxial stress temperature measurement (BSTM) were conducted from room temperature up to 650° C during the heating and the cooling cycle. In general, a BSTM cycle for TiN/Cu shows the following features: in the as-deposited state, the coatings show tensile stresses. During heating, these stresses relax and become compressive due to the different thermal expansion coefficient of coating and substrate. Above a certain temperature, which depends on the kind of coating, a plateau develops and the stress level remains constant up to the maximum annealing temperature. The plateau is related to plastic deformation of Cu, which relieves all further stresses, and to defect annihilation of TiN, occurring near the maximum heating temperature. During cooling, the coatings exhibit linear thermo-elastic behaviour, but due to high tensile stresses cracks or plastic deformation of Cu occur near

room temperature. Stress levels during heating depend on the thickness of the Cu-layer for bi-layers, on the bi-layer thickness Λ for multilayers (the thinner Λ the higher) and on the Cu content for nanocomposite coatings (increasing Cu content results in higher tensile stress). For bi-layered and multilayered coatings there is a special effect after cooling. The thinner the Cu layer in bi-layers and the thinner Λ in multilayers is the higher are the tensile stresses at room temperature. This might be related to hardening effects in very thin films due to grain refinement. For nanocomposites, the coating with 14 at.% Cu behaves totally different. It exhibits in the as-deposited state very high compressive stresses which might be related to a fully percolated nanocomposite structure. Stress increases with increasing temperature and the curve does not show a plateau due to plastic deformation of Cu, but the relaxation of stresses in TiN due to defect annihilation is very pronounced for this coating.

Tribological properties of nanocomposites evaluated at different temperatures depend on the Cu content in the coating. At room temperature, wear is mainly caused by abrasion through micro-ploughing and micro-cutting. The coefficient of friction for nanocomposites slightly decreases with increasing Cu content, but is higher than that of TiN. Friction and wear behaviour are influenced by oxidation of the coating. Especially for coatings with Cu contents $\geq 19\text{at.}\%$, oxidised material is back-transferred to the wear track and protects the coating during the experiment. In case of the nanocomposite with 30 at.% Cu, the coating fails as a result of its inferior mechanical properties and less effective protection by oxide scales. At elevated temperatures, oxidation becomes the most significant feature and increases with temperature as well as with Cu content. Wear seems to be induced by mild abrasion. At 500° C, the coefficient of friction is lower than at room temperature and it slightly decreases with increasing Cu content. This might be referred to the deteriorating mechanical properties and oxide formation.

In summary, this thesis summarizes the effect of Cu addition in different arrangements (i.e. bi-layers, multilayers and nanocomposites) to sputtered TiN films on structure, stress and stress relaxation and in the case of nanocomposites, also on tribological properties. Further investigations might be executed on those TiN/Cu nanocomposites, which are assumed to have fully percolated structures, thus showing the most promising properties.

REFERENCES

- [1] **M. Ohring**, The Materials Science of Thin Films, Academic Press, London (1992)
- [2] **S. PalDey, S. C. Deevi**, Mater. Sci. Engin. A 342 (2003) 58
- [3] **A. Cavaleiro, B. Trindade, M. T. Vieira**, in Nanostructured Coatings, edited by A. Cavaleiro, J. Th. M. De Hosson, Springer, New York, 2006
- [4] **S. J. Bull**, Vacuum 43 (1992) 387
- [5] **S. J. Bull, D. S. Rickby**, Mat. Res. Soc. Symp. Proc. 188 (1990) 337
- [6] **C. Mitterer, P. H. Mayrhofer, J. Musil**, Vacuum 71 (2003) 279
- [7] **S. Vepřek, S. Reiprich**, Thin Solid Films 268 (1995) 64
- [8] **J. Musil**, Surf. Coat. Technol. 125 (2000) 322
- [9] **J. Musil, P. Zeman, H. Hruby, P. H. Mayrhofer**, Surf. Coat. Technol. 120-121 (1999) 179
- [10] **H. Köstenbauer, G. A. Fontalvo, G. Hlawacek, C. Teichert, J. Keckes, C. Mitterer**, J. Nanoscience Nanotechnol., accepted
- [11] **L. Hultman, C. Mitterer**, in Nanostructured Coatings, edited by A. Cavaleiro, J. Th. M. De Hosson, Springer, New York, 2006
- [12] **H. Köstenbauer, G. A. Fontalvo, J. Keckes, C. Mitterer**, Thin Solid Films 516 (2008) 1920
- [13] **P. H. Mayrhofer**, Lecture Script Basics of Deposition and Materials Science of Hard Coatings, University of Leoben (2004)
- [14] **R. F. Bunshah**, Deposition Technologies, Properties and Applications, Noyes Publications, New Jersey (2001)
- [15] **Fr.-W. Bach, T. Duda**, Moderne Beschichtungsverfahren, Wiley VCH, Weinheim (2000)
- [16] **K.-P. Müller**, Praktische Oberflächentechnik, Vieweg, Braunschweig / Wiesbaden (1996)
- [17] **E. Moll**, in Advanced Techniques for Surface Engineering, edited W. Gissler, H. A. Jehn, Kluwer Academic Publishers, Dordrecht (1992)
- [18] **K. W. Mertz, H. A. Jehn**, Praxishandbuch moderne Beschichtungen, Hanser Verlag, München (2001)
- [19] **G. Kienel, K. Röhl**, Vakuumbeschichtung 2, Verfahren und Anlagen, VDI – Verlag, Düsseldorf (1995)
- [20] **D. M. Mattox**, in Plasma Surface Engineering Volume 1, edited E. Broszeit, W. D. Münz, H. Oechsner, K.-T. Rie, G. K. Wolf, DGM, Oberursel (1989)
- [21] **B. Rother, J. Vetter**, Plasmabeschichtungsverfahren und Hartstoffschichten, Deutscher Verlag für Grundstoffindustrie, Leipzig (1992)
- [22] **A. Grill**, Cold Plasma in Materials Fabrication, IEEE Press, New York, (1994)
- [23] **B. Chapman**, Glow Discharge Processes, John Wiley, New York (1980)

-
- [24] **R. A. Haefler**, Oberflächen- und Dünnschicht-Technologie Teil I, Springer, Heidelberg (1987)
- [25] **D. M. Mattox**, Handbook of Physical Vapor Deposition (PVD) Processing, Noyes Publications, Westwood (1998)
- [26] **J. L. Vossen, W. Kern**, Thin Film Processes II, Academic Press, Boston (1991)
- [27] **H. Frey**, Vakuumbeschichtung 1, Plasmaphysik – Plasmadiagnostik - Analytik, VDI - Verlag, Düsseldorf (1995)
- [28] **P. H. Mayerhofer**, Materials Science Aspects of Nanocrystalline PVD Hard Coatings, Dissertation, Montanuniversität Leoben (2001)
- [29] **M. S. Wong, W. D. Sproul, S. L. Rohde**, Surf. Coat. Technol. 49 (1991) 121
- [30] **Y. Pauleau**, in Advanced Techniques for Surface Engineering, edited W. Gissler, H. A. Jehn, Kluwer Academic Publishers, Dordrecht (1992)
- [31] **R. P. Howson, H. A. J'Afer, A. G. Spencer**, Thin Solid Films 193/194 (1990) 127
- [32] **S. M. Rossnagel, J. J. Cuomo**; Vacuum 38 (1988) 2
- [33] **P. Panjan, B. Navinšek, A. Žabkar**, in Plasma Surface Engineering Volume 2, edited E. Broszeit, W. D. Münz, H. Oechsner, K.-T. Rie, G. K. Wolf, DGM, Oberursel (1989)
- [34] **W. D. Sproul, P. J. Rudnik**, Surf. Coat. Technol. 39/40 (1989) 499
- [35] **J. A. Venables, G. D. T. Spiller, M. Hanbücken**, Rep. Prog. Phys. 47 (1984) 399
- [36] **H. A. Jehn**, in Advanced Techniques for Surface Engineering, edited W. Gissler, H. A. Jehn, Kluwer Academic Publishers, Dordrecht (1992)
- [37] **J. E. Greene**, in Handbook of Crystal Growth, Vol.1, edited D.T.J Hurle, Elsevier, Amsterdam (1993)
- [38] **R. D. Bland, G. J. Kominiak, D. M. Mattox**, J. Vac. Sci. Technol., 11 (4) (1974) 671
- [39] **K. Kutschej**, Wear Resistant, Low Friction Hard Coatings for Cutting Applications, Dissertation, Montanuniversität Leoben (2005)
- [40] **B. A. Movchan, A. V. Demchishin**, Phys. Met. Metallogr. 28 (4) (1969) 83
- [41] **R. Messier, A. P. Giri, R. A. Roy**, J. Vac. Sci. Technol. A 2 (1984) 500
- [42] **J. A. Thornton**, J. Vac. Sci. Technol. 11 (4) (1974) 666
- [43] **J. A. Thornton**, Ann. Rev. Mater. Sci. 7 (1977) 239
- [44] **P. B. Barna, M. Adamik**, in Protective Coatings and Thin Films, edited Y. Pauleau, P. B. Barna, Kluwer Academic Publishers, Dordrecht (1997)
- [45] **W. D. Callister, Jr.**, Materials Science and Engineering, John Wiley, New York (2000)
- [46] **H. Willmann**, Al-Cr-N Thin Film Design for High Temperatures Applications, Dissertation, Montanuniversität Leoben (2007)
- [47] **P. Haasen**, Physical Metallurgy, Cambridge University Press, Cambridge (1996)
- [48] **G. Gottstein**, Physikalische Grundlagen der Materialkunde, Springer, Berlin (2007)
- [49] **R. E. Smallman, R. J. Bishop**, Modern Physical Metallurgy & Materials Engineering, Elsevier, Oxford (1999)
- [50] **E. Arzt**, Acta Mater. 46 (1998) 5611
-

-
- [51] **C. Suryanarayana**, *International Materials Reviews* 40 (1995) 41
- [52] **H. Hahn, K. A. Padmanabhan**, *NanoStructured Materials* 6 (1995) 191
- [53] **S. Yip**, *Nature* 5 (1998) 532
- [54] **S. C. Tjong, H. Chen**, *Materials Science and Engineering R* 45 (2004) 1
- [55] **R. W. Siegel, G. E. Fougere**, *NanoStructured Materials* 6 (1995) 205
- [56] **H. Gleiter**, *Acta Mater.* 48 (2000) 1
- [57] **J. Patscheider, T. Zehnder, M. Diserens**, *Surf. Coat. Technol.* 146-147 (2001) 201
- [58] **A. D. Korotaev, A. N. Tyumentsev, Yu. P. Pinzhin, G. E. Remnev**, *Surf. Coat. Technol.* 185 (2004) 38
- [59] **W. Schatt, H. Worch**, *Werkstoffwissenschaft*, Deutscher Verlag für Grundstoffindustrie, Stuttgart (1996)
- [60] **M. F. Ashby, D. R. H. Jones**, *Engineering Materials 2*, Butterworth-Heinemann, Oxford (2006)
- [61] **H. Köstenbauer**, *Fundamental Investigations on Stress Engineering of Sputtered Hard Coatings*, Dissertation, Montanuniversität Leoben (2008)
- [62] **D. M. Mattox**, *J. Vac. Sci. Technol. A* 7 (1989) 1105
- [63] **E. S. Machlin**, *Materials Science in Microelectronics*, Giro Press, New York (1995)
- [64] **L. B. Freund, S. Suresh**, *Thin Film Materials, Stress, Defect Formation and Surface Evolution*, Cambridge University Press, Cambridge (2003)
- [65] **F. Spaepen**, *Acta Mater.* 48 (2000) 31
- [66] **W. D. Nix**, *Metallurg. Trans. A* 20 (1989) 2217
- [67] **H. Oettel, R. Wiedemann, S. Preißler**, *Surf. Coat. Technol.* 74-75 (1995) 273
- [68] **G. G. Stoney**, *Proc. Roy. Soc. Lond. A* 82 (1909) 172
- [69] **C. Kajdas**, in *Tribology Science and Application*, edited M. A. Herman, F. Franek, C. Kajdas, PAN (2003)
- [70] **K. Holmberg, A. Matthwes**, *Coatings Tribology, Properties, Techniques and Applications in Surface Engineering*, Elsevier, Amsterdam (1994)
- [71] **K.-H. Zum Gahr**, *Microstructure and Wear of Materials*, Elsevier, Amsterdam (1987)
- [72] **B. Bhushan**, *Principles and Applications of Tribology*, John Wiley, New York (1999)
- [73] **D. T. Gawne**, in *Surface Engineering Casebook Solutions to Corrosion and Wear-related Failures*, edited by J.S. Burnell-Gray, P.K. Datta, Woodhead Publishing, Cambridge (1996)
- [74] **H. Jehn**, *Charakterisierung dünner Schichten*, Beuth Verlag, Berlin (1993)
- [75] **L. I. Tushinsky, I. Kovensky, A. Plokhov, V. Sindeyev, P. Reshedka**, *Coated Metal – Structure and Properties of Metal-Coating Compositions*, Springer, Berlin (2002)
- [76] **D. C. Joy**, in *Electron Microscopy - Principles and Fundamentals*, edited by S. Amelinckx, D. van Dyck, J. van Landuyt, G. van Tendeloo, Wiley-VCH, Weinheim (1997)
- [77] **B. E. Warren**, *X-Ray Diffraction*, Dover Publications, New York (1990)

-
- [78] **M. Birkholz**, Thin Film Analysis by X-Ray Scattering, Wiley-VCH, Weinheim (2006)
- [79] **Wikipedia Contributors**, Transmission electron microscopy, Wikipedia, The Free Encyclopedia (7 May 2008)
http://en.wikipedia.org/w/index.php?title=Transmission_electron_microscopy&oldid=210763382
- [80] **D. J. O'Connor, B. A. Sexton, R. St. C. Smart**, Surface Analysis Methods in Materials Science, Springer, Berlin (2003)
- [81] IBIS User Guide, Fischer Cripps Laboratory
- [82] **NanoFocus Bedienungsanleitung**, Nanofocus AG, Oberhausen (2003)
- [83] **Wikipedia Contributors**, Confocal laser scanning microscopy, Wikipedia, The Free Encyclopedia (22 April 2008)
http://en.wikipedia.org/w/index.php?title=Confocal_laser_scanning_microscopy&oldid=207385160
- [84] **Th. H. Keijser, J. I. Langford, E. J. Mittemeijer, A. B. P. Vogels**, J. Appl. Cryst. 15 (1982) 308
- [85] **P. H. Mayrhofer, C. Mitterer, L. Hultman, H. Clemens**, Progr. Mater. Sci. 51 (2006) 1032
- [86] **C. Mitterer, P. H. Mayrhofer**, Key Engineering Materials 264-268 (2004) 453
- [87] **H. Köstenbauer, G. A. Fontalvo, M. Kapp, J. Keckes, C. Mitterer**, Surf. Coat. Technol. 201 (2007) 4777
- [88] **J.-E. Sundgren, H. T. G. Hentzell**, J. Vac. Sci. Technol. A 4 (5) (1986) 2259
- [89] **F. H. Stott**, Tribology International 31 (1998)61
- [90] **A. Matthews, S. Franklin and K. Holmberg**, J. Phys. D: Appl Phys. 40 (2007) 5463